Inorganic Chemistry

Article

pubs.acs.org/IC

3d4f Heterobimetallic Dinuclear and Tetranuclear Complexes Involving Tetrathiafulvalene as Ligands: X-ray Structures and Magnetic and Photophysical Investigations

Goulven Cosquer, Fabrice Pointillart,* Boris Le Guennic, Yann Le Gal, Stéphane Golhen, Olivier Cador, and Lahcène Ouahab*

Institut des Sciences Chimiques de Rennes, UMR 6226 CNRS, Université de Rennes 1, 263 Avenue du Général Leclerc, 35042 Rennes Cedex, France

Supporting Information

ABSTRACT: Six new 3d4f heterobimetallic dinuclear complexes, $[(\mathbf{L^1})MLn(hfac)_3]$ [M = Cu^{II}, Ni^{II}; Ln = Y^{III}, Er^{III}, Yb^{III}; $\mathbf{L^1}$ = 4,5-bis(propylthio)tetrathiafulvalene-*N*,*N*′-phenylenebis(salicylideneimine) and $hfac^-$ = 1,1,1,5,5,5-hexafluoroacetylacetonate], and one tetranuclear complex, $[(\mathbf{L^2})Cu(OH)Er(hfac)_3]_2$ (where $\mathbf{L^2}$ = 4,5-bis(propylthio)-tetrathiafulvalene-*N*,*N*′-phenyleneaminosalicylideneimine), have been synthesized. All of the X-ray structures of the coordination complexes have been resolved from single-crystal diffraction. A quantitative magnetic approach has allowed one to determine the Cu−Ln ferromagnetic interaction for Gd^{III} (1.29 cm^{-1}) and Tb^{III} (0.40 cm^{-1}) and the antiferromagnetic interaction for Dy^{III} (−0.46 cm^{-1}) and Yb^{III} (−2.25 cm^{-1}), while in the case of Er^{III}, the magnetic interactions are negligible. The UV−visible absorption properties have been studied in a chloroform solution and rationalized by DFT and TD-DFT calculations. Upon oxidation, intramolecular SOMO → LUMO (20800 cm^{-1}) and SOMO−*n* → SOMO (11350 cm^{-1}) charge transfers appear, while the HOMO → LUMO charge transfers (20750 cm^{-1}) disappear. The reversibility of the oxidation has been confirmed by electrochemistry and absorption properties upon the addition of a reducing agent. Irradiation at the HOMO → LUMO charge-transfer energy of the dinuclear complex $[(\mathbf{L^1})NiY(hfac)_3]$ induces a ligand-centered fluorescence at 14450 cm^{-1}.

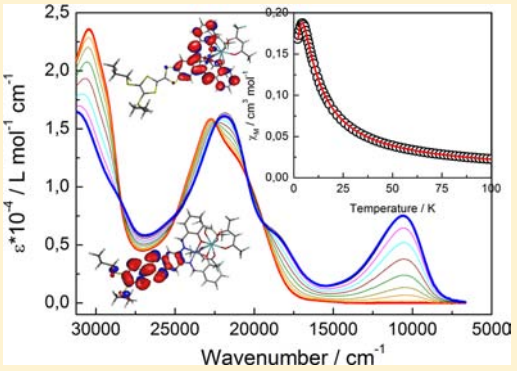

INTRODUCTION

Because of their strongly electron-donating and attractive reversible redox properties, tetrathiafulvalene (TTF) and its derivatives are used successfully as building blocks for molecular conductors,[1] molecular switches,[2] and solar-energy systems.[3] Nowadays, the challenge of this chemistry is to succeed the combination or the synergy between several properties to reach the elaboration of multifunctional materials.[4] Thus, one strategy consists of the combination of TTF derivatives with 3d or 4f metal ions to take advantage of their magnetic and optical properties, giving rise to the original "*π*-3d",[5] "*π*-4f",[6] or "*π*-3d4f"[7] complexes. Such systems can be obtained either by a "through-space" or a "through-bond" approach. In the former, the metallic ion and the TTF core interact through van der Waals contacts, while in the latter, the metallic ion and the TTF core are covalently linked by a chemical bridge. Using the second approach, the first 3d4f TTF-based heterobimetallic complexes were elaborated[7] to combine the strong Ising-type magnetic anisotropy[8] of the Dy^{III} and Tb^{III} ions and the enhancement of the intramolecular magnetic-exchange interactions when such ions are combined with 3d ions.[9]

Besides their magnetic properties, another advantage of lanthanides lies in their specific luminescence properties with, among others, potential applications in chelate lasers,[10] efficient organic light-emitting diodes (OLEDs),[11] and polymer light-emitting diodes (PLEDs).[12]

Following this strategy, we decided to extend the series of 3d4f coordination complexes with the near-infrared (NIR)-emitters Er^{III} and Yb^{III} ions associated with the $[M(\mathbf{L^1})]$ metallic precursors [where M = Cu^{II} and Ni^{II} and $\mathbf{L^1}$ = 4,5-bis(propylthio)tetrathiafulvalene-*N*,*N*′-phenylenebis-(salicylideneimine); Scheme 1]. The diamagnetic Y^{III} analogue has also been studied in order to perform quantum-chemical calculations and to corroborate the absorption properties. The obtained complexes have the following molecular formula: $[(\mathbf{L^1})]MLn(hfac)_3]$ [M = Cu^{II} and Ln = Y^{III} (**1**), Er^{III} (**2**), Yb^{III} (**3**); M = Ni^{II} and Ln = Y^{III} (**4**), Er^{III} (**5**), Yb^{III} (**6**), where $hfac^-$ = 1,1,1,5,5,5-hexafluoroacetylacetonate anion]. The monosubstitution of the 4,5-bis(propylthio)tetrathiafulvalene-*N*,*N*′-phenylene unit with a salicylideneimine leads to the new ligand [$\mathbf{L^2}$ = 4,5-bis(propylthio)tetrathiafulvalene-*N*,*N*′-phenyl-

Received: May 22, 2012
Published: July 11, 2012

dx.doi.org/10.1021/ic3010689 | *Inorg. Chem.* 2012, 51, 8488−8501

Scheme 1. Synthetic Procedures for L^1 and L^2

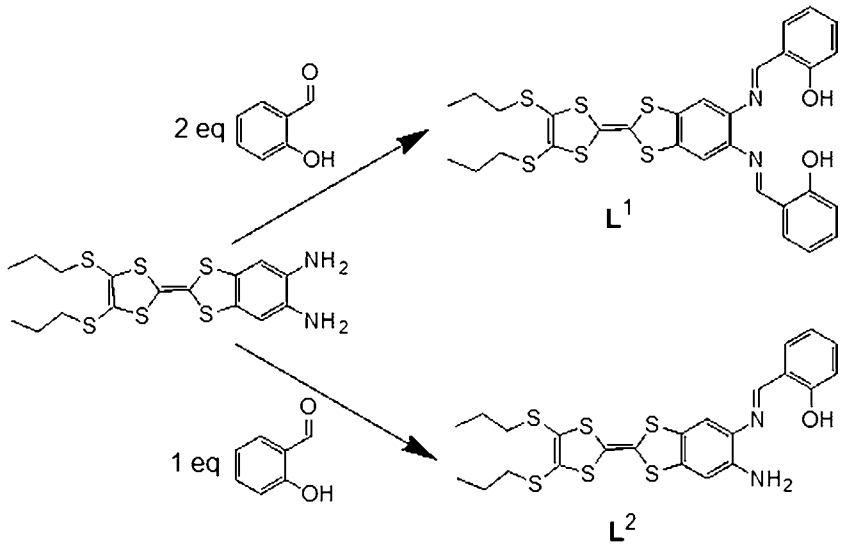

Table 1. Crystallographic Data for Compounds 3, 4, and 7

	$(L^1)CuYb(hfac)_3$ (3)	$(L^1)NiY(hfac)_3$ (4)	$[(L^2)Cu(OH)Er(hfac)_3]_2$ (7)
formula	$C_{45}H_{29}CuF_{18}N_2O_8S_6Yb$	$C_{45}H_{29}F_{18}N_2NiO_8S_6Y$	$C_{76}H_{52}Cu_2Er_2F_{36}N_4O_{16}S_{12}$
M/g mol^{-1}	1496.7	1407.68	2805.6
cryst syst	triclinic	triclinic	triclinic
space group	$P\bar{1}$ (No. 2)	$P\bar{1}$ (No. 2)	$P\bar{1}$ (No. 2)
cell param	a = 12.5872(8) Å	a = 13.2766(6) Å	a = 12.8981(13) Å
	b = 13.7283(9) Å	b = 13.3127(10) Å	b = 13.7598(16) Å
	c = 17.4659(8) Å	c = 16.5097(13) Å	c = 18.7360(20) Å
	α = 87.316(4)°	α = 85.513(4)°	α = 93.903(4)°
	β = 88.101(4)°	β = 77.716(4)°	β = 95.854(5)°
	γ = 66.921(2)°	γ = 84.331(4)°	γ = 111.867(5)°
volume/Å^3	2773.2(3)	2832.4(3)	3049.5(6)
Z	2	2	1
T/K	293(2)	293(2)	293(2)
2θ range/deg	4.50 ≤ 2θ ≤ 50.78	5.92 ≤ 2θ ≤ 49.54	4.32 ≤ 2θ ≤ 50.90
ρ_{calc}/g cm^{-3}	1.791	1.651	1.527
μ/mm^{-1}	2.397	1.682	2.017
no. of reflns	15432	14453	17037
indep reflns	9464	8869	10434
R_{int}	0.0383	0.0486	0.0627
$F_o^2 > 2\sigma(F_o)^2$	6789	5091	5711
no. of variables	905	899	646
R1, wR2	0.0456, 0.1065	0.0517, 0.1149	0.0607, 0.1355

eneaminosalicylideneimine; Scheme 1]. The treatment of L^2 by 3d Cu^{II} and 4f Er^{III} gives the tetranuclear complex of formula $[Cu(L^2)(OH)Er(hfac)_3]_2$ (7).

The magnetic properties of the whole series of complexes were studied and the nature of the interaction determined using an quantitative method. The optical properties were measured and discussed upon oxidation and reduction.

EXPERIMENTAL SECTION

General Procedures and Materials. All solvents were dried using standard procedures. 4,5-Bis(propylthio)tetrathiafulvalene-*N*,*N*′-phenylenebis(salicylideneimine) (L^1),[13] M-4,5-bis(propylthio)-tetrathiafulvalene-*N*,*N*′-phenylenebis(salicylideneimine)[13] [$M(L^1)$] (M = Cu, Ni), and $Ln(hfac)_3{\cdot}2H_2O$[14] (Ln = Y, Er, Yb) compounds were prepared according to literature procedures. All other reagents were purchased from Aldrich Co. Ltd. and were used without further purification.

Crystallography. Single crystals were mounted on a Nonius four-circle diffractometer equipped with a CCD camera and a graphite-monochromated Mo Kα radiation source (λ = 0.71073 Å), from the Centre de Diffractométrie (CDIFX), Université de Rennes 1, Rennes, France. Data were collected at 293 K. Structures were solved with a direct method using the *SIR-97* program and refined with a full-matrix least-squares method on F^2 using the *SHELXL-97* program.[15] Crystallographic data are summarized in Table 1. Because of the disorder and the large thermal factors of the propyl groups at 293 K, the C atoms of these groups were refined isotropically for 7. A *SQUEEZE* procedure was realized. Data are listed for all voids in the P1 unit cell, i.e., center of gravity, solvent-accessible volume, recovered number of electrons in the void (90 electrons, corresponding to a *n*-hexane molecule), and details about the squeezed material are given in the CIF file.

Physical Measurements. Cyclic voltammetry was carried out in a CH_2Cl_2 solution, containing 0.1 M $(C_4H_9)_4NPF_6$ as the supporting electrolyte. Voltammograms were recorded at 100 mV s^{-1} at a

dx.doi.org/10.1021/ic3010689 | Inorg. Chem. 2012, 51, 8488−8501

Table 2. Cell Parameters for Compounds 1, 2, 5, and 6

	$(L^1)CuY(hfac)_3$ (1)	$(L^1)CuEr(hfac)_3$ (2)	$(L^1)NiEr(hfac)_3$ (5)	$(L^1)NiYb(hfac)_3$ (6)
formula	$C_{45}H_{29}CuF_{18}N_2O_8S_6Y$	$C_{45}H_{29}CuErF_{18}N_2O_8S_6$	$C_{45}H_{29}ErF_{18}N_2NiO_8S_6$	$C_{45}H_{29}F_{18}N_2NiO_8S_6Yb$
M/g mol^{-1}	1411.4	1489.8	1485.0	1490.7
cryst syst	triclinic	triclinic	triclinic	triclinic
space group	$P\bar{1}$ (No. 2)	$P\bar{1}$ (No. 2)	$P\bar{1}$ (No. 2)	$P\bar{1}$ (No. 2)
cell parameters	a = 12.66(5) Å	a = 12.636(50) Å	a = 13.00(5) Å	a = 13.11(4) Å
	b = 13.75(5) Å	b = 13.828(50) Å	b = 13.52(5) Å	b = 13.37(2) Å
	c = 17.51(7) Å	c = 17.495(70) Å	c = 16.50(6) Å	c = 16.51(6) Å
	α = 86.55(4)°	α = 86.99(4)°	α = 77.316(3)°	α = 77.23(4)°
	β = 87.99(4)°	β = 87.30(4)°	β = 87.239(5)°	β = 87.40(5)°
	γ = 67.17(2)°	γ = 66.18(2)°	γ = 86.021(5)°	γ = 86.00(5)°
volume/Å^3	2804(19)	2791(2)	2821(18)	2814(14)
T/K	293(2)	293(2)	293(2)	293(2)

platinum disk electrode. The potentials were measured versus a saturated calomel electrode (SCE; Table 4). Optical spectra were measured using a KBr disk method on a Perkin-Elmer 1600 Series Fourier transform infrared spectrometer (resolution 4 cm^{-1}) for IR. Absorption spectra were recorded on a Varian Cary 5000 UV–visible–NIR spectrometer. The luminescence spectra were measured using a Horiba-Jobin Yvon Fluorolog-3 spectrofluorimeter, equipped with a three-slit double-grating excitation and emission monochromator with dispersions of 2.1 nm mm^{-1} (1200 grooves mm^{-1}). The steady-state luminescence was excited by unpolarized light from a 450 W xenon continuous-wave lamp and detected at an angle of 90° for diluted solution measurements or at 22.5° for solid-state measurement (front-face detection) by a Peltier-cooled red-sensitive Hamamatsu R2658P photomultiplier tube (300–1010 nm). Spectra were reference-corrected for both the excitation source light-intensity variation (lamp and grating) and the emission spectral response (detector and grating). Uncorrected NIR spectra were recorded at an angle of 45° using a liquid-nitrogen-cooled, solid indium/gallium/arsenic detector (850–1600 nm). The direct-current magnetic susceptibility measurements were performed on a solid polycrystalline sample with a Quantum Design MPMS-XL SQUID magnetometer between 2 and 300 K in applied magnetic fields of 0.2 T for temperatures of 2–20 K and 1 T for temperatures of 20–300 K. The experimental data were corrected from the diamagnetism of the sample holder, and the intrinsic diamagnetism of the materials was evaluated with Pascal's tables.

Computational Details. Density functional theory (DFT) geometry optimizations and time-dependent DFT (TD-DFT) excitation energy calculations of the ligand L^1, 3d metalloprecursor $[(L^1)Ni]$, and 3d4f heterobimetallic dinuclear analogue **4** were carried out with the *Gaussian 09* (revision A.02) package[16] employing the PBE0 hybrid functional.[17] The "Stuttgart/Dresden" basis sets and effective-core potentials were used to describe the Y atom,[18] whereas all other atoms were described with the SVP basis sets.[19] The differences with a triple-ζ quality basis set were probed on the ligands, and they are meaningless. The first 50 monoelectronic excitations were calculated for L^1 and $[(L^1)Ni]$, and 110 excitations were necessary for complex **4**. In all steps, a modeling of bulk solvent effects (solvent = chloroform) was included through the polarizable continuum model (PCM),[20] using a linear-response nonequilibrium approach for the TD-DFT step.[21] Molecular orbitals (MOs) were sketched using the *Gabedit* graphical interface.[22]

Synthesis of the Ligand L^2 and Complexes 1–7. *4,5-Bis(propylthio)tetrathiafulvalene-N,N′-phenyleneaminosalicylideneimine (L^2).* Salicylaldehyde (0.256 g, 2.1 mmol) was slowly added to a CH_2Cl_2/CH_3CN (1:3) solution of 5,6-diamino-2-[4,5-bis(propylthio)-1,3-dithio-2-ylidene]benzone[*d*]-1,3-dithiole (0.909 g, 2.1 mmol) and stirred overnight. The resulting precipitate was filtered and washed with ethanol. The ligand was obtained as an orange powder and used without purification for complexation with a Cu^{II} ion. Yield: 1.05 g (93%).

$[(L^1)CuY(hfac)_3]$ (1). A 10 mL $CHCl_3$ solution of $[(L^1)Cu]$ (15 mg, 0.021 mmol) and $Y(hfac)_3{\cdot}2H_2O$ (15.7 mg, 0.021 mmol) was stirred for 1 h. *n*-Heptane was layered to the solution, and dark-red crystals of **1** were obtained after 1 week of slow evaporation. Yield: 11.7 mg (39%). IR: 2965, 1652, 1609, 1531, 1510, 1458, 1370, 1257, 1202, 1144, 912, 800, 757, 660, 587 cm^{-1}.

$[(L^1)CuEr(hfac)_3]$ (2). Single crystals of **2** were obtained by a method similar to that for **1** starting from $Er(hfac)_3{\cdot}2H_2O$ (17.3 mg, 0.021 mmol) instead of $Y(hfac)_3{\cdot}2H_2O$. Yield: 15.4 mg (49%). IR: 2969, 1652, 1608, 1530, 1509, 1459, 1370, 1256, 1200, 1143, 912, 799, 757, 659, 586 cm^{-1}.

$[(L^1)CuYb(hfac)_3]$ (3). Single crystals of **3** were obtained by a method similar to that for **1** starting from $Yb(hfac)_3{\cdot}2H_2O$ (17.4 mg, 0.021 mmol) instead of $Y(hfac)_3{\cdot}2H_2O$. Yield: 6.2 mg (20%). IR: 2969, 1669, 1652, 1608, 1542, 1509, 1458, 1370, 1257, 1203, 1144, 799, 758, 660, 586 cm^{-1}.

$[(L^1)NiY(hfac)_3]$ (4). A 10 mL $CHCl_3$ solution of $[(L^1)Ni]$ (14.6 mg, 0.021 mmol) and $Y(hfac)_3{\cdot}2H_2O$ (15.7 mg, 0.021 mmol) was stirred for 1 h. *n*-Heptane was added to the solution, and crystals were obtained after 1 week of slow evaporation. Yield: 8.1 mg (27%). IR: 2969, 1652, 1608, 1530, 1509, 1458, 1370, 1257, 1202, 1144, 799, 758, 660, 586 cm^{-1}.

$[(L^1)NiEr(hfac)_3]$ (5). Single crystals of **5** were obtained by a method similar to that for **4** starting from $Er(hfac)_3{\cdot}2H_2O$ (17.3 mg, 0.021 mmol) instead of $Y(hfac)_3{\cdot}2H_2O$. Yield: 12.0 mg (38%). IR: 2967, 1669, 1652, 1608, 1531, 1508, 1458, 1365, 1292, 1257, 1203, 1145, 800, 757, 660, 587 cm^{-1}.

$[(L^1)NiYb(hfac)_3]$ (6). Single crystals of **6** were obtained by a method similar to that for **4** starting from $Yb(hfac)_3{\cdot}2H_2O$ (17.5 mg, 0.021 mmol) instead of $Y(hfac)_3{\cdot}2H_2O$. Yield: 8.1 mg (27%). IR: 2967, 1669, 1653, 1608, 1531, 1506, 1458, 1365, 1292, 1257, 1205, 1145, 800, 757, 660, 587 cm^{-1}.

$[(L^2)Cu]$. A 20 mL CH_3CN solution of $Cu(OAc)_2{\cdot}nH_2O$ (37.2 mg, 0,186 mmol) was added to a 20 mL CH_2Cl_2 solution of L^2 (100 mg, 0.186 mmol). After 12 h of stirring, the precipitate was collected and washed with ethanol. Yield: 109 mg (98%).

$[(L^2)Cu(OH)Er(hfac)_3]_2$ (7). A 5 mL $CHCl_3$ solution of $Er(hfac)_3{\cdot}2H_2O$ (20.6 mg, 0,025 mmol) was added to a 10 mL $CHCl_3$ solution of $[(L^2)Cu]$ (15 mg, 0,025 mmol) and stirred for 1 h. *n*-Hexane was layered to the solution, and red crystals of **7** were obtained after 1 week of slow evaporation. Yield: 11.6 mg (31%).

RESULTS AND DISCUSSION

Synthesis. The 3d4f heterobimetallic dinuclear complexes **1–6** were obtained following a previously published method,[7] which consists of coordination of the Lewis acid $Ln(hfac)_3{\cdot}2H_2O$ (Ln = Y, Er, Yb) to the metallic Lewis base $[(L^1)M]$ (M = Cu, Ni). A modification of the synthesis of L^1 consisting of the slow addition of 1 equiv of salycylaldehyde to 5,6-diamino-2-[4,5-bis(propylthio)-1,3-dithio-2-ylidene]-benzone[*d*]-1,3-dithiole permits one to obtain the monosubstituted ligand L^2 (Scheme 1). The reaction between the Lewis

dx.doi.org/10.1021/ic3010689 | Inorg. Chem. 2012, 51, 8488–8501

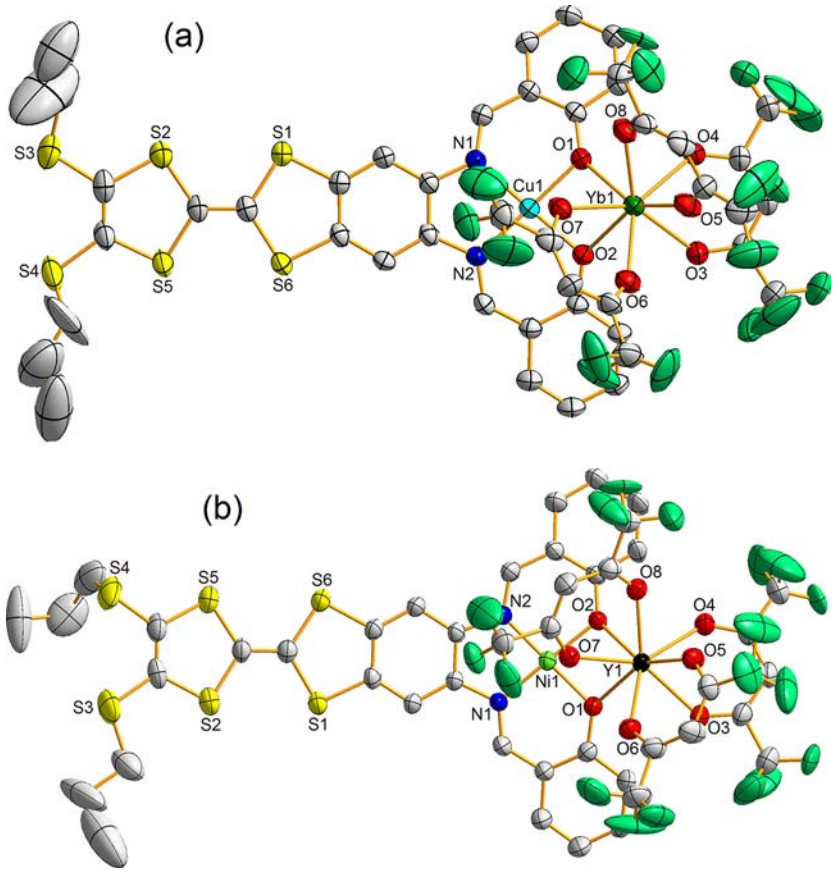

Figure 1. ORTEP views of the asymmetric units of **3** (a) and **4** (b). Thermal ellipsoids are drawn at 30% probability. H atoms are omitted for clarity. In the case of **3**, only the three hfac$^-$ ions with the highest occupation factors are represented.

acid Er(hfac)$_3$·2H$_2$O and the Lewis base [(**L**^{2})Cu] leads to the unprecedented 3d4f heterobimetallic tetranuclear complex **7**.

Crystal-Structure Analysis of [(L^1)CuYb(hfac)$_3$] (3) and [(L^1)NiY(hfac)$_3$] (4). Our previous work has shown that two structural families built from the Cu^{II} and Ni^{II} ions can be obtained, respectively.[7] The refinements of the X-ray structures of **3** and **4** were done to be representative of each of these families (Table 1). The structures of the other members of each family were checked by determination of the cell parameters (Table 2).

Both compounds crystallize in the triclinic $P\bar{1}$ (No. 2) space group (Table 1). The asymmetric unit is composed of one [(**L**^{1})M] and one Ln(hfac)$_3$ moieties linked by two bridging phenolate groups (Figure 1). The Cu and Ni ions are in a N_2O_2 inner coordination site, connected in a square-planar environment to the two amine N and two phenoxo O atoms from the **L**^{1} ligand. The average values of Cu−O [1.921(4) Å] and Cu−N [1.928(5) Å] bond lengths are longer than the corresponding ones for Ni^{II} [1.869(3) and 1.850(4) Å] in agreement with the electronic configuration of the 3d ions (Table 3). Ln ions are in a slightly distorted bicapped square-faced trigonal-prismatic coordination sphere made of eight O atoms that arise from three bis-chelating hfac$^-$ anions and one bis-chelating [(**L**^{1})M] metalloligand. The coordination polyhedron has a C_{2v} symmetry.

The central C11−C12 bond lengths of the TTF fragment are 1.334(9) Å for **3** and 1.332(8) Å for **4**. The arrangement of the propyl groups is different in **3** and **4** (Figure 1) and leads to the formation of different crystal packings. In **3**, dimers of **L**^{1} donors constitute the organic network (Figure S1 in the Supporting Information), while in **4**, a reminiscent organic network is observed with S···S contacts (Figure S2 in the Supporting Information). The Cu^{II} ion interacts with two O and N atoms in the axial positions, while the Ni^{II} ion realizes only one axial contact with one O atom.

Table 3. Selected Bond Lengths (Å) for 3, 4, and 7[a]

	3	4	7
M−O1	1.926(4)	1.873(3)	1.926(5)
M−O2	1.916(4)	1.865(3)	1.934(5)
M−N1	1.935(5)	1.846(4)	1.920(6)
M−N2	1.920(5)	1.853(4)	1.989(7)
Ln−O1	2.356(4)	2.413(4)	2.424(5)
Ln−O2	2.346(4)	2.416(3)	2.431(5)
Ln−O2^i			2.357(5)
Ln−O3	2.285(5)	2.358(4)	2.443(7)
Ln−O4	2.287(5)	2.335(4)	2.384(7)
Ln−O5	2.278(6)	2.325(4)	2.387(6)
Ln−O6	2.315(5)	2.325(4)	2.344(6)
Ln−O7	2.314(5)	2.336(4)	2.427(6)
Ln−O8	2.345(5)	2.321(4)	2.394(6)
M1−Ln1	3.185(10)	3.219(10)	3.262(11)

[a] i: $-x, -y, -z$.

Compound 7. **7** crystallizes in the triclinic $P\bar{1}$ (No. 2) space group (Table 1). The asymmetric unit is composed of one [(**L**^{2})Cu] metalloprecursor and one Er(hfac)$_3$ unit. The two moieties are linked by one bridging phenolate (O1) and one μ_3-hydroxo (O2) groups. The inversion center generates a heterobimetallic tetranuclear compound with the two Er^{III} ions

dx.doi.org/10.1021/ic3010689 | Inorg. Chem. 2012, 51, 8488−8501

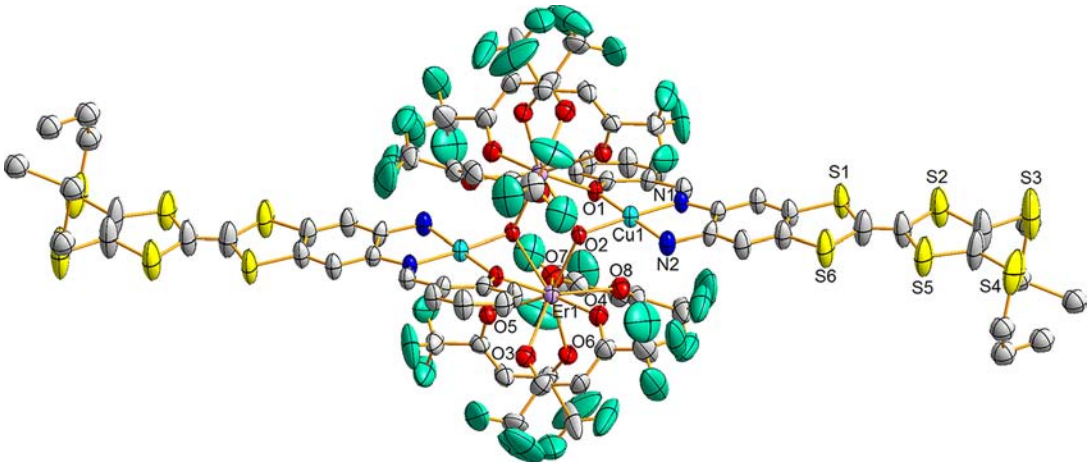

Figure 2. ORTEP view of the molecular structure of **7**. Thermal ellipsoids are drawn at 30% probability. H atoms and thermal ellipsoids for the propyl groups are omitted for clarity.

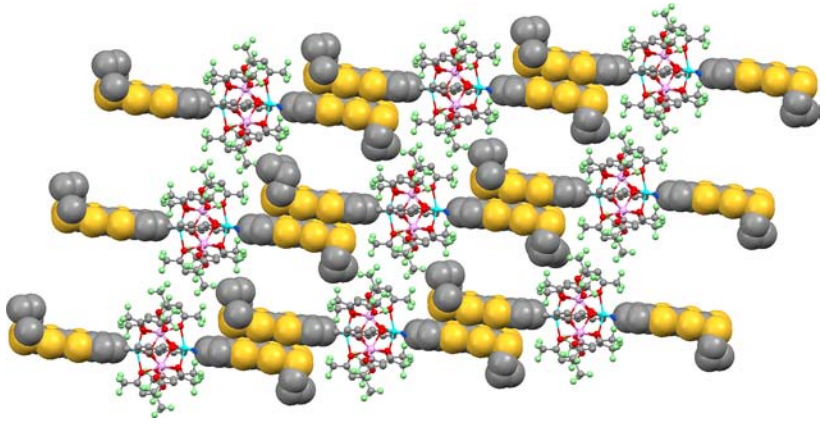

Figure 3. Crystal packing of **7** highlighting the formation of $\mathbf{L}^2$ dimers (space-fill representation) and inorganic networks (ball-and-stick representation).

bridged by two μ_3-OH (Figure 2). The Cu ions are in a N_2O_2 inner coordination site, connected in a square-planar environment to two N atoms and one phenoxo O atom coming from the $\mathbf{L}^2$ ligand and one hydroxo O atom. The average Cu−O and Cu−N distances are 1.930(5) and 1.955(7) Å, respectively (Table 3). The Cu−O distances are homogeneous, while the Cu−N2 bond length is longer than the Cu−N1 one because N2 is doubly protonated (amine) and N1 is not protonated (imine). The Cu^{II} ion performs short contacts with two O atoms coming from $hfac^-$ anions in the axial positions [Cu1−O5 = 2.575(6) Å and Cu1−O8 = 2.553(6) Å].

The Er^{III} centers are nine-coordinated, and the Er−O distances range from 2.344(6) to 2.443(7) Å (Table 3). The arrangement of the linked ligands leads to coordination polyhedra, which can be described as a distorted four-capped square antiprism with 14 triangular faces.[23] The two propyl groups of $\mathbf{L}^2$ are oriented on the same side of the plane formed by the TTF core. This arrangement leads to the formation of "head-to-tail" dimers of $\mathbf{L}^2$ (Figure 3), but no short S···S contacts are found in these dimers because the shortest S2···S6 and S1···S5 contacts are found equal to 3.901 and 3.994 Å. This situation is probably due to the big size of the Cu_2Er_2 cluster constituting the inorganic network (Figure 3). In the inorganic cluster, the shortest Cu···Cu, Cu···Er, and Er···Er distances were measured as 5.605, 3.263, and 3.965 Å, respectively. The respective shortest intermolecular distances were found to be equal to 9.123, 10.109, and 11.336 Å.

Large voids were observed between the dimers of donors (Figure 3), giving rise to channels (Figure S3 in the Supporting Information) that are filled by *n*-hexane molecules.

Electrochemical Properties. The redox properties of complexes **2**, **5**, and **7** are investigated by cyclic voltammetry.

The cyclic votammograms for the dinuclear and tetranuclear complexes show two monoelectronic oxidations at 0.637 and 1.003 V for **2**, 0.638 and 0.999 V for **5**, and 0.621 and 0.988 V for **7**. They correspond successively to the formation of the TTF fragment radical cation and dication (Figure S4 in the Supporting Information). Oxidation potentials are shifted to higher positive values relative to the parent TTF due to partial electron transfer from the donor (TTF) to the *N*,*N*′-phenylenbis(salicylideneimine) or *N*,*N*′-phenyleneaminosalicylideneimine acceptor moiety. The values of the oxidation potentials are in agreement with those previously found for the $[(\mathbf{L}^1)M]$ (M = Cu^{II}, Ni^{II})[13] and $[(\mathbf{L}^1)MLn(hfac)_3]$ (Ln = Gd^{III}, Tb^{III}, Dy^{III})[7] complexes. Only a very weak decrease of the electron transfer from the TTF core to the acceptor is observed in $\mathbf{L}^2$ compared to $\mathbf{L}^1$. Nevertheless, the electrochemical properties attest to the redox activity of the complexes. Such redox properties are required to play a role as molecular precursors for 3d4f heterobimetallic conducting magnets.

dx.doi.org/10.1021/ic3010689 | *Inorg. Chem.* 2012, 51, 8488−8501

Magnetic Properties. *Dinuclear Complexes [(L¹)MLn(hfac)₃].* The temperature dependence of the χ_M, $\chi_M T$ being the molar magnetic susceptibility, of compound **3** is represented in Figure 4. At room temperature, $\chi_M T$ is equal to 2.74 cm^3 K mol^{-1}. This value is slightly smaller than expected for two uncoupled magnetic moments arising from Cu^{II} (0.413 cm^3 K mol^{-1} with g_{Cu} = 2.1) and Yb^{III} (2.57 cm^3 K mol^{-1} for the ground-state multiplet $^2F_{7/2}$ with $g_{7/2} = {}^8/_7$).[24a] Upon cooling, $\chi_M T$ decreases slightly down to 20 K (~1.6 cm^3 K mol^{-1}) and more abruptly upon cooling further down to 2 K (0.34 cm^3 K mol^{-1}). While the slight decrease upon cooling from room temperature is commonly observed and is related to the splitting of the ground-state multiplet of lanthanide due to the local crystal field, the abrupt decrease below 20 K can only be due to interactions between the magnetic moments of the ground-state multiplet $^2F_{7/2}$ of Yb^{III} and the spin $^1/_2$ of Cu^{II}. Surprisingly, the molar magnetic susceptibility χ_M passes through a broad maximum at T_{max} = 4.2 K (Figure 4), which cannot be ascribed to an antiferromagnetic−paramagnetic phase transition owing to the large shortest intermolecular distance between magnetic moments (~10 Å). Then, the maximum arises from the compensation between the local magnetic moments of the two metals in a dimer. Owing to the presence of a large kinetic orbital moment, the quantitative interpretation of the magnetism of lanthanide-containing dimers is not straightforward, while a comparative method in 3d4f systems between the magnetic and nonmagnetic 3d-substituted ion gives efficient qualitative information on the nature of magnetic interactions between 3d and 4f ions. We thus wrote a program to fit the magnetic susceptibility in 3d4f systems. The complete Hamiltonian to be considered is reported in the Supporting Information. The Hamiltonian, with nine parameters to describe the zero-field splitting of any lanthanide, is written for a symmetry environment as low as C_{2v}. Because it is unrealistic to fit the data with nine parameters, we decided then to fit the temperature dependence of the magnetic susceptibility considering the high D_{4d} symmetry environment. In this case, only four or five parameters, B_2^0, B_4^0 (B_6^0), and J, and a small amount of paramagnetic impurities, χ_{imp}, have to be taken into account (eq 1).

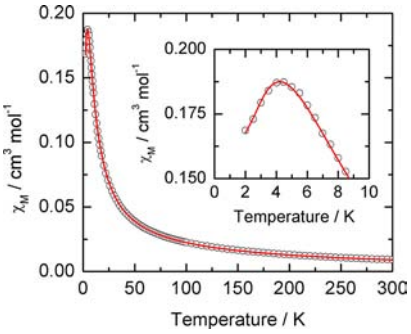

Figure 4. Temperature dependence of the molar magnetic susceptibility, χ_M, for a powdered sample of compound **3** with a zoom on the low-temperature range in the inset. The best-fitted curve (see the text) is represented by the red line.

$$\hat{H} = B_2^0\widehat{O_2^0} + B_4^0\widehat{O_4^0} + B_6^0\widehat{O_6^0} + \beta(g_J\hat{J} + g_s\hat{S})\cdot\vec{H} - J\hat{J}\cdot\hat{S} \quad (1)$$

The first three terms corresponds to the crystal-field effects with $\hat{O}_k^q$ the operator equivalents, which can be expressed as polynomials of the total angular momentum matrixes (J^2, J_z, J_+, and J_-),[25] whereas the following terms correspond to the Zeeman effect on the lanthanide and spin-only magnetic moments, which are coupled through J. Parameters of interest are the B_k^q's (numerical parameters) and J. The magnetization is first calculated for three orientations (x, y, and z) of a given magnetic field; then the magnetic susceptibility is calculated by dividing by the amplitude of the applied field and averaging over the three directions. Temperature dependences of χ_M and $\chi_M T$ can thus be fitted. The best fit was obtained with J = −2.2537(1) cm^{-1}, g_s = 2.1 (fixed), B_2^0 = 1.327(3) cm^{-1}, B_4^0 = −0.4717(2) cm^{-1}, and χ_{imp} = 0.09669 cm^3 K mol^{-1} (see Figure 4). The agreement is very good, especially in the low-temperature range, where we were able to reproduce T_{max}. A better agreement was obtained in the high-temperature region upon fitting the $\chi_M T$ vs T curve [J = −2.1188(6) cm^{-1}, g_s = 2.1 (fixed), B_2^0 = 4.982(3) cm^{-1}, B_4^0 = −0.34705(6) cm^{-1}, and χ_{imp} = 0.042(4) cm^3 K mol^{-1}]. With these two sets of parameters, the ground state of Yb^{III} unambiguously corresponds to M_J = $\pm{}^1/_2$, while excited states are located a few hundred wavenumbers above (Table 4). The total splitting (~600 cm^{-1}) is in agreement with the splitting of the ground-state multiplet observed in a low-symmetry environment by luminescence.[26] At room temperature, the thermal energy is equal to 210 cm^{-1}; therefore, the uncertainty on the energies of the highest M_J states is very large, and so they must be considered with caution.

Table 4. Calculated Energy Levels (cm^{-1}) of the M_J States for Yb^{III} in Compound 3 with the Two Sets of Parameters from the Fit of χ_M and $\chi_M T$ vs T Curves

M_J	B_2^0 = 1.327(3) cm^{-1}	B_2^0 = 4.982(3) cm^{-1}
	B_4^0 = −0.4717(2) cm^{-1}	B_4^0 = −0.34705(6) cm^{-1}
$\pm{}^1/_2$	0	0
$\pm{}^7/_2$	104	221
$\pm{}^3/_2$	347	280
$\pm{}^5/_2$	647	547

With the fitted set of parameters, we can simulate the field dependence of the magnetization (Figure 5). The simulation reproduces fairly well the experimental curve, especially the change of curvature at high field. The energies of the first four levels calculated for the dimer with J = −2.2537(1) cm^{-1}, B_2^0 = 1.327(3) cm^{-1}, and B_4^0 = −0.4717(2) cm^{-1} are represented in Figure 6. The eigenvectors are linear combinations of vectors

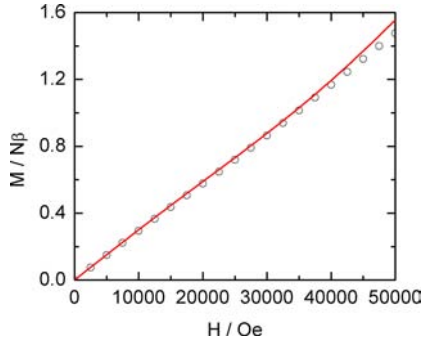

Figure 5. Magnetic field dependence of the magnetization of a powdered sample of compound **3** measured at 2 K, with the simulated curve obtained with the set of parameters given in the main text.

dx.doi.org/10.1021/ic3010689 | Inorg. Chem. 2012, 51, 8488−8501

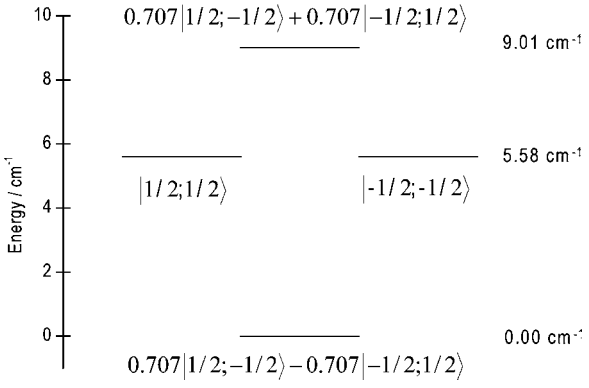

Figure 6. First four energy levels calculated in zero field for compound **3** with $J = -2.2537$ cm^{-1}, $B_2^0 = 1.3271$ cm^{-1}, and $B_4^0 = -0.47176$ cm^{-1} with the eigenvectors on the basis of $|M_J; M_S\rangle$.

$|M_J; M_S\rangle$ with $M_J = \pm^7/_2, \pm^5/_2, \pm^3/_2, \pm^1/_2$ and $M_S = \pm^1/_2$ for Ln and Cu^{II}, respectively. These levels correspond only to coupling between $M_J = \pm^1/_2$ of Yb^{III} and $M_S = \pm^1/_2$ of Cu^{II}. Therefore, this energy diagram is identical with the energy diagram in the case of anisotropic coupling between two spins $^1/_2$. With the help of the Pauli matrixes, it is not difficult to demonstrate that the first four levels can be reproduced with the Hamiltonian $H = -JS_1 \cdot S_2$ with $J_z = J$ and $J_x = J_y = 4J$. The spin operators S_1 and S_2 have their usual meaning. Of course, the simulation of the magnetic data with this simple model, only valid when the ground state is populated, requires the effective Zeeman factors $g_z = g_J$, $g_x = g_y = 4g_J$ for Yb^{III} and $g = 2.1$ for Cu^{II} (Figure S5 in the Supporting Information).

The $\chi_M T$ vs T curves for the Er^{III} compounds **2** and **5** are plotted in Figure 7. In the whole temperature range, $\chi_M T$ of **2** is

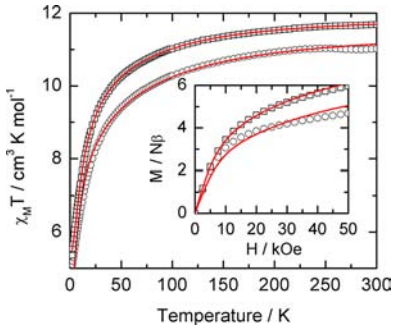

Figure 7. $\chi_M T$ vs T curves for compounds **5** (circles) and **2** (squares), with the best-fitted curves using the model described in the text (red lines). The inset shows the field dependences of the magnetization at 2 K for **5** (circles) and **2** (squares), with the simulated curves (red lines) using parameters from the fits.

stronger than that for **5**. The substitution of the magnetic ion Cu^{II} by the diamagnetic Ni^{II} decreases, as expected, the effective moment. The model proposed here above can be applied to these two systems: one (**5**) consists of a Er^{III} ion ($^4I_{15/2}$) in a C_{2v} environment, while the other (**2**) consists of a Er^{III} ion in a C_{2v} environment coupled with a spin $^1/_2$. The best-fitted parameters are grouped together in Table 5. Two points must be raised: (1) Fitted parameters are close in **2** and **5** as a consequence of identical coordination polyhedra around the Er^{III} ion in the two compounds; (2) the magnetization curves are fairly well reproduced for both compounds. A small ferromagnetic coupling exists in **2**, about 5 times smaller than

Table 5. Best-Fitted Parameters for Compounds 5, 2, and 3

	5 (NiEr)	**2** (CuEr)	**3** (CuYb)
g_J	$^6/_5$ (fixed)	$^6/_5$ (fixed)	$^8/_7$ (fixed)
g_S		2.1 (fixed)	2.1 fixed
B_2^0	1.6898(6) cm^{-1}	1.5096(2) cm^{-1}	1.327(3) cm^{-1}
B_4^0	0.02814(1) cm^{-1}	0.02124(2) cm^{-1}	−0.4717(2) cm^{-1}
J		0.3955(3) cm^{-1}	−2.2537(1) cm^{-1}

the antiferromagnetic coupling found in **3**. Analysis of the wave functions reveals that the ground state of Er^{III} corresponds to the $M_J = \pm^9/_2$ state, while the highest state in the $^4I_{15/2}$ multiplet corresponds to $M_J = \pm^{15}/_2$ and is located about 600 cm^{-1} above the ground state (see Figure S6 in the Supporting Information). Here again the uncertainty resides on the exact position of the highest states (~400 cm^{-1} above the ground state), which are not accessible with thermal excitation at room temperature.

We then decided to reinvestigate in a quantitative manner the magnetism of the Dy and Tb analogues of compounds **2** and **5**.[7] In ref 7, the comparative method was successfully employed to determine the nature (ferro- or antiferromagnetic) of the interaction between Cu^{II} and Dy^{III} and between Cu^{II} and Tb^{III}. Antiferromagnetic interactions operate in the Cu−Dy dimer and ferromagnetic in the Cu−Tb dimer. The fitting of the magnetic data with the model used for compounds **2** and **5** provides quantitative information on the amplitude of the interaction (Figure S7 in the Supporting Information). However, we have to add a third parameter, B_6^0, to reproduce satisfactorily both $\chi_M T$ vs T and M vs H curves. The procedure is to fit first the Ni^{II} analogue with the zero-field-splitting parameters and then to inject these parameters (fixed) in the fitting of the Cu^{II} analogue; then the only free parameter remains the interaction between the magnetic centers. Unambiguously, ferromagnetic interactions operate in Gd^{III} [7] (+1.29 cm^{-1}) and Tb^{III} (+0.40 cm^{-1}) derivatives, while antiferromagnetic interactions operate in Dy^{III} (−0.46 cm^{-1}) and Yb^{III} (−2.25 cm^{-1}) compounds. In the Er^{III} derivative, the interaction can be considered negligible.

Our quantitative approach confirms the results obtained with the qualitative empirical method previously reported, i.e., the ferromagnetic interactions taking place between both Tb^{III} and Cu^{II} ions.[7] In other heterobimetallic Cu−Dy complexes, it turns out that the nature of the superexchange interaction, or at least its amplitude, is related to the dihedral angle Dy−O1−O2−Cu: the smaller this angle is, the smaller is the ferromagnetic interaction in amplitude. The interaction appears to be very small in amplitude for an angle close to 135°, while it is unambiguously ferromagnetic for angle values higher than 150°.[27,28] Nevertheless, in the latter case, the value of the magnetic-exchange interaction depends not only on the dihedral angle value but also on the Stevens operators (symmetry around the Ln ion).[25] Until now, no examples close to our heterobimetallic compounds were published with a similar angle value and symmetry, and consequently it is difficult to perform suitable comparisons. The magnetic studies of the nature of the interaction between the Cu^{II} and Yb^{III}/Er^{III} ions are scarce. In the case of Yb^{III}, the reported examples deal with dihedral angle values close to 180°. Even if the angle value and symmetry seem to be comparable in the reported examples, the nature of the interaction between the Cu^{II} and Yb^{III} ions were found to be ferromagnetic[27c] and antiferromagnetic.[27b] In conclusion in our systems, the Cu−Ln interaction is

dx.doi.org/10.1021/ic3010689 | Inorg. Chem. 2012, 51, 8488−8501

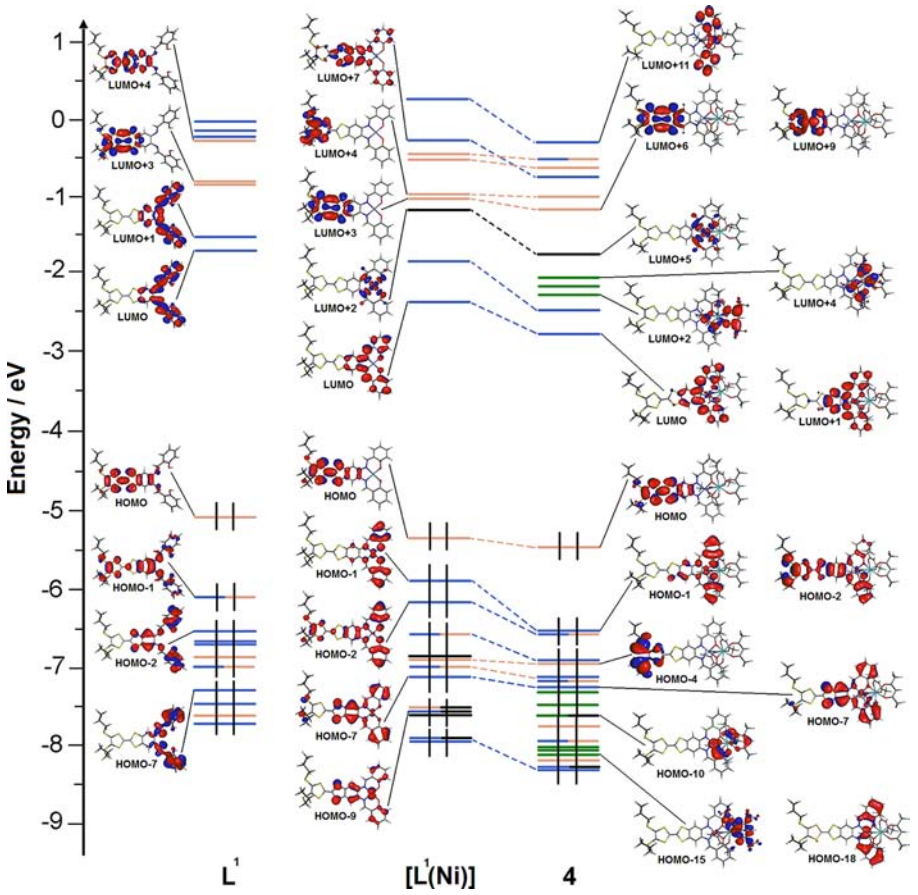

Figure 8. MO diagrams of $\mathbf{L^1}$, [($\mathbf{L^1}$)Ni], and **4**. The energy levels of the centered TTF, salphen, Ni^{II}, and $hfac^-$ orbitals are respectively represented in orange, blue, black, and green.

ferromagnetic for Ln = Gd and Tb and antiferromagnetic for Ln = Dy and Yb, while it is complicated to conclude in the case of the Er^{III} ion.

Tetranuclear Complex **7**. The room temperature $\chi_M T$ for compound **7** is equal to 23.07 cm^3 K mol^{-1}, which is slightly lower than the expected value for two $^4I_{15/2}$ multiplets with g_J = 6/5 and two $S = {}^1/_2$ ($_{gCu}$ = 2.1). $\chi_M T$ decreases monotonically upon cooling to reach 10.5 cm^3 K mol^{-1} at 2 K, while the magnetization does not saturate under 50 kOe at 2 K (Figure S8 in the Supporting Information). Owing to the structural complexity of compound **7**, it is difficult to analyze precisely its magnetism: (1) The distance between the Er^{III} ions is so short that we cannot neglect interactions between lanthanides, at least of dipolar origin; (2) the coordination number and therefore the polyhedron around lanthanide are different with respect to compounds **2** and **5** changing the zero-field-splitting parameters; (3) a superexchange interaction between Cu^{II} and Er^{III} ions also exists.

Photophysical Properties. *Absorption Properties.* The experimental absorption properties of the free ligand $\mathbf{L^1}$ and the metallic precursors [($\mathbf{L^1}$)M] were previously studied in solution.[7,13] The MO diagrams were obtained by DFT (see the Experimental Section) for $\mathbf{L^1}$, [($\mathbf{L^1}$)Ni], and **4** (Figure 8 and Table 6). To support and rationalize the experimental attributions and observations, TD-DFT calculations (see the Experimental Section) were also performed (Figure 9 and Table 6). The experimental absorption spectrum of **4** is depicted in Figure 10.

The experimental absorption curve of $\mathbf{L^1}$ was previously deconvoluted in five bands.[7] The calculated UV−visible absorption spectrum for $\mathbf{L^1}$ well reproduces the experimental $\mathbf{L^1}$ curve (Figure 9). The lowest-energy band was calculated at the average value of 23256 cm^{-1} (experimental value found at 25400 cm^{-1}) and attributed to $\pi-\pi^*$ HOMO → LUMO (96%) (22783 cm^{-1}) + HOMO → LUMO +1 (81%) (23728 cm^{-1}) TTF donor to salphen acceptor charge transfers ($DACT^1$; Table 6). The absorption band centered at 29900 cm^{-1} has been calculated at the average value of 30479 cm^{-1} and attributed to the $\pi-\pi^*$ HOMO−1 → LUMO (81%) (28943 cm^{-1}) + HOMO−1 → LUMO+1 (68%) (30554 cm^{-1}) and HOMO−2 → LUMO+1 (46%) + HOMO−1 → LUMO +1 (18%) (31939 cm^{-1}) intrasalphen transitions and salphen to phenol CTs (Table 6). The next absorption band centered at 33000 cm^{-1} was identified as the HOMO → LUMO+4 (71%) intra-TTF (ID) transition (32675 cm^{-1}; Table 6). The Gaussian deconvolution centered at 36000 cm^{-1} was calculated at 35320 cm^{-1}, attributed to several CTs involving the TTF core, salphen acceptor, and phenyldiimine moiety, and mainly described by the HOMO−1 → LUMO +3 (28%) + HOMO → LUMO +5 (25%) transitions (Table 6). The highest-energy large absorption band at 42400 cm^{-1} corresponds to the three excitations calculated at 38081, 38537, and 40928 cm^{-1}, i.e., the $\pi-\pi^*$ HOMO−7 → LUMO (38%) + HOMO−7→ LUMO+1 (26%) + HOMO−1→ LUMO+5 (53%) intrasalphen transitions (Table 6).

After metalation by the Ni^{II} ion, the lowest-energy CTs ($DACT^1$) were calculated at the average energy of 20542 cm^{-1}

dx.doi.org/10.1021/ic3010689 | *Inorg. Chem.* 2012, 51, 8488−8501

Table 6. TD-DFT-Calculated Excitation Energies and Main Compositions of Low-Lying Electronic Transitions Associated with an Oscillator Strength $f > 0.10$, 0.08, and 0.05, Respectively, for L^1, $[(L^1)Ni]$, and 4[a]

	energy (cm^{-1})					
	exptl	theor	osc	type	assignment	transition
L^1	25400[b]	22783	0.15	DACT[1]	$\pi_{TTF} \rightarrow \pi^*_{salphen}$	H → L (96%)
		23728	0.25			H → L+1 (81%)
	29900[b]	28943	0.22	IA	$\pi_{salphen} \rightarrow \pi^*_{salphen} + \pi_{salphen} \rightarrow \pi^*_{phenol}$	H−1 → L (81%)
		30554	0.36			H−1 → L+1 (68%)
		31939	0.12			H−1 → L+1 (18%)
						H−2 → L (46%)
	33000[b]	32675	0.84	ID	$\pi_{TTF} \rightarrow \pi^*_{TTF}$	H → L+4 (71%)
	36000[b]	35320	0.18	ILCT	$\pi_{salphen} \rightarrow \sigma^*_{TTF}$	H−1 → L+3 (28%)
					$\pi_{TTF} \rightarrow \pi^*_{salphen}$	H → L+5 (25%)
	42400[b]	38081	0.16	IA	$\pi_{salphen} \rightarrow \pi^*_{salphen}$	H−7 → L (38%)
		38537	0.13	IA		H−7 → L+1 (26%)
		40928	0.11	IA	$\pi_{salphen} \rightarrow \pi^*_{salphen}$	H−1 → L+5 (53%)
$[(L^1)Ni]$	20200[b]	19688	0.09	DACT[1]	$\pi_{TTF} \rightarrow \pi^*_{salphen}$	H → L (95%)
	22500[b]	21396	0.21			H → L+1 (85%)
		22048	0.49	IA	$\pi_{salphen} \rightarrow \pi^*_{salphen}$	H−1 → L (85%)
	26900[b]	28410	*c*	LMCT	$\pi_{TTF} \rightarrow d_{x^2-y^2(Ni)}$	H → L+2 (72%)
	29900[b]	27513	0.29	IA	$\pi_{salphen} \rightarrow \pi^*_{salphen}$	H−2 → L+1 (95%)
		28898	0.49			H−3 → L (76%)
		31745	0.57			H−7 → L (71%)
	32800[b]	33373	0.19	ID	$\pi_{TTF} \rightarrow \pi^*_{TTF}$	H → L+5/+6 (31/14%)
	37500[b]	34911	0.30	ID	$\pi_{TTF} \rightarrow \pi^*_{TTF}$	H → L+5 (15%)
				MLCT	$d_{xz(Ni)} \rightarrow \pi^*_{salphen}$	H−9 → L (35%)
		35682	0.09	ID	$\pi_{TTF} \rightarrow \pi^*_{TTF}$	H → L+6 (31%)
				ILCT	$\pi_{salphen/TTF} \rightarrow \sigma^*_{TTF}$	H−2 → L+3 (25%)
		38158	0.08	ILCT	$\pi_{salphen/TTF} \rightarrow \pi^*_{TTF}$	H−2 → L+4 (51%)
	43100[b]	40077	0.09	IA	$\pi_{salphen} \rightarrow \pi^*_{salphen}$	H−1 → L+7 (81%)
4	19500	17568	0.05	DACT[1]	$\pi_{TTF} \rightarrow \pi^*_{salphen}$	H → L (97%)
	22000	19807	0.33			H → L+1 (98%)
	26600	24080	0.27	IA	$\pi_{salphen} \rightarrow \pi^*_{salphen}$	H−1 → L (88%)
		25129	*c*	LMCT	$\pi_{TTF} \rightarrow d_{x^2-y^2(Ni)}$	H → L+5 (78%)
	30100	27815	0.29	IA + ILCT	$\pi_{salphen} \rightarrow \pi^*_{salphen} + \pi_{salphen/TTF} \rightarrow \pi^*_{salphen}$	H−2 → L+1 (81%)
		28373	0.11			H−3/−5 → L(36/21%)
		30302	0.54			H−4/−7 → L(32/41%)
		31228	0.14			H−4/−6/−7 → L (27/18/33%)
	32700	33927	0.08	ID + ILCT + Ihfac	$\pi_{TTF} \rightarrow \pi^*_{TTF} + \pi_{TTF} \rightarrow \pi^*_{salphen} + \pi_{salphen} \rightarrow \sigma^*_{TTF} + \pi_{hfac} \rightarrow \pi^*_{hfac}$	H−6 → L+1 (19%)
						H → L+9 (27%)
		35002	0.08			H−12 → L (17%)
						H−8 → L+2 (25%)
						H−5 → L+4 (13%)
		36097	0.13			H → L+9 (16%)
						H−2 → L+6 (19%)
	37600	37969	0.06	ILCT + Ihfac	$\pi_{TTF} \rightarrow \pi^*_{salphen} + \pi_{hfac/d_z^2(Ni)} \rightarrow \pi^*_{hfac} + \pi_{hfac} \rightarrow \pi^*_{hfac}$	H−11 → L+1 (16%)
						H−10 → L+2 (12%)
						H−9 → L+4 (27%)
		38721	0.11			H → L+11 (14%)
						H−10 → L+3/+4 (29/15%)
		39202	0.10			H−10 → L+4 (33%)
		39931	0.08			H−13/−15 → L+2 (21/28%)
	42800	40365	0.06	IA	$\pi_{salphen} \rightarrow \pi^*_{salphen}$	H−18 → L+1 (24%)

[a]In addition, the charge-transfer and pure intramolecular transitions are reported. ID, IA, and $Ihfac^-$ and H, L, and nb represent respectively the intramolecular TTF (donor), salphen (acceptor), and $hfac^-$ transitions and HOMO and LUMO; therefore, DACT and ILCT stand for the donor-to-acceptor and intraligand charge transfers. The theoretical values are evaluated at the PCM($CHCl_3$)−PBE0/SVP level of approximation. [b]Data given from this reference. [c]The oscillator strength has been calculated to be very low because of the long-range character of these CT bands and the absence of overlap between the TTF-centered orbitals and the Ni^{II}-centered $d_{x^2-y^2}$ orbital.

dx.doi.org/10.1021/ic3010689 | Inorg. Chem. 2012, 51, 8488−8501

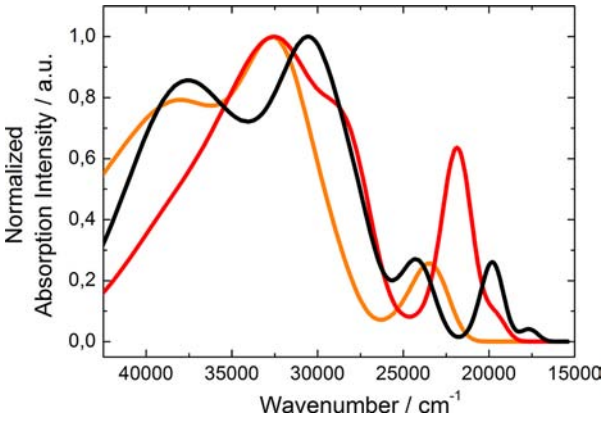

Figure 9. Theoretical absorption spectra of compounds $\mathbf{L^1}$ (orange line), [($\mathbf{L^1}$)Ni] (red line), and **4** (black line).

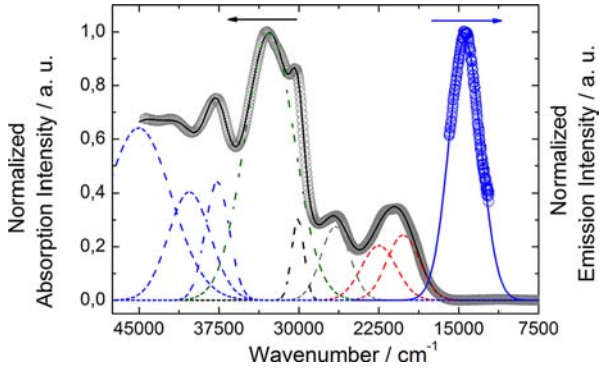

Figure 10. Experimental dichloromethane solution (4×10^{-5} M) UV−visible absorption spectra (open gray circles), Gaussian deconvolutions (dashed lines), best fit (full black line; R = 0.9997), and fluorescence (open blue circles) with its extrapolation (full blue line) for **4**.

(experimental value found at 21350 cm^{-1}) and were attributed to $\pi-\pi^*$ HOMO → LUMO (95%) (19688 cm^{-1}) + HOMO → LUMO+1 (85%) (21396 cm^{-1}) TTF-to-salphen^{2-} CTs (DACT^1; Table 6). The experimental energy stabilization of 4000 cm^{-1} due to Ni^{II} coordination was theoretically evaluated to 2700 cm^{-1}. The red shift of DACT^1 is due to a simultaneous energy stabilization of 0.22 and 0.66 eV of the HOMO and LUMO, which are centered on the TTF and salphen^{2-} units respectively (Figure 8). It is worth noticing that a strong $\pi-\pi^*$ contribution centered on the salphen^{2-} acceptor appeared after metalation of $\mathbf{L^1}$ [HOMO−1 → LUMO (85%), 22048 cm^{-1}]. The expected ligand-to-metal CT (LMCT; 26900 cm^{-1}) was calculated at 28410 cm^{-1} and attributed to the π^*_{TTF} → $d_{x2-y2(Ni)}$ HOMO → LUMO+2 (72%) transition. The $\pi-\pi^*$ intrasalphen^{2-} transitions for [($\mathbf{L^1}$)Ni] were calculated to the average energy of 29395 cm^{-1}, which is almost the same energy as that for the free ligand. The main responsible excitations for this absorption band are HOMO−2 → LUMO+1 (95%) (27513 cm^{-1}) + HOMO-3 → LUMO (76%) (28898 cm^{-1}) and HOMO−7 → LUMO (71%) (31745 cm^{-1}; Table 6). The following two experimental absorption bands (32800 and 37500 cm^{-1}) were attributed to the $\pi-\pi^*$ intra-TTF HOMO → LUMO+5/+6 excitations (34655 cm^{-1}) and $\pi-\sigma^*/\pi-\pi^*$ HOMO−2 → LUMO+3/+4 salphen^{2-}-to-TTF CTs (36920 cm^{-1}). Compared to the free ligand, an additional metal-to-ligand CT (MLCT) was identified at 34911 cm^{-1} and attributed to the $d_{xz(Ni)} \rightarrow \pi^*_{salphen}$ HOMO−9 → LUMO transition. Finally, the highest energy absorption band was again attributed to $\pi-\pi^*$ intrasalphen^{2-} transitions (40077 cm^{-1}).

Coordination of the Y(hfac)$_3$ unit leads to an additional 1850 cm^{-1} red shift of the DACT^1 bands [experimental red deconvolution in Figure 10; HOMO → LUMO (97%) (17568 cm^{-1}) + HOMO → LUMO+1 (98%) (19807 cm^{-1})]. The energy stabilization of the HOMO and LUMO orbitals is equal to 0.13 and 0.40 eV, respectively (Figure 8). In other words, the electronic withdrawing of the Y(hfac)$_3$ unit is weaker than the Ni^{II} one. This can be explained by two reasons: (i) the Y(hfac)$_3$ unit is far from the TTF core and (ii) the Ni^{II} ion is coordinated through the two phenolate groups and the two imine groups, while the Y(hfac)$_3$ unit is only coordinated through the phenolate groups. Nevertheless, the energy stabilization of the TTF-centered orbitals after 4f coordination attests to the good electronic communication between both the TTF core and Y^{III} metal center. The low-energy $\pi-\pi^*$ IA transitions [HOMO−1 → LUMO (88%)] and LMCT [HOMO → LUMO +5 (78%)] bands are now calculated at 24080 and 25129 cm^{-1}. The LMCT energy is calculated lower in **4** than in [($\mathbf{L^1}$)Ni] because of the strong stabilization of the Ni^{II}-centered $d_{x^2-y^2}$ orbital after Y^{III} coordination (Figure 8). The decrease of the electron density on the salphen^{2-} fragment after 4f coordination favors the appearance of TTF → salphen^{2-} CT (ILCT) instead of IA and ID transitions (cf. $\mathbf{L^1}$ and [($\mathbf{L^1}$)Ni] attributions) because salphen^{2-} is a better acceptor in **4** than in the metalloprecursor. Thus, the black deconvolution (30100 cm^{-1}; Figure 10) was attributed to the calculated HOMO−2 → LUMO+1 (81%) (27815 cm^{-1}) and HOMO−3/−4/−5/−6/−7 → LUMO (average value of 29968 cm^{-1}) transitions (Table 6). The green deconvolution (Figure 10) involves ID + ILCT and the intra-hfac$^-$ bands, with their calculated energies being in the range from 33927 to 36097 cm^{-1} (Table 6). The hfac$^-$-centered transitions were calculated at higher energy compared to the energy usually obtained experimentally for such transitions (32700 cm^{-1}).[61] The hfac$^-$ contributions come from two kinds of transitions: (i) HOMO−10 → LUMO+2/+3/+4 excitations (calculated energies from 37969 to 39202 cm^{-1}); (ii) HOMO−13/−15 → LUMO+2 excitations (39931 cm^{-1}). Concerning the HOMO−10 orbital, a strong contribution of the filled d_{z^2} Ni^{II}-centered orbital was found (Figure 8). Finally, the highest-energy deconvolution was attributed to IA transitions, which were associated with HOMO−18 → LUMO+1 (24%) (40365 cm^{-1}).

The free ligand $\mathbf{L^1}$ (Figure S9 in the Supporting Information), metallic precursors [M$\mathbf{L^1}$] [M = Cu^{II} (Figure S10 in the Supporting Information), Ni^{II} (Figure S11 in the Supporting Information)], Cu^{II}- and Ni^{II}-based dinuclear complexes [**3** (Figure S12 in the Supporting Information) and **4** (Figure 11)], and the tetranuclear complex **7** (Figure 12) were studied upon the addition of different amounts of $NOPF_6$ oxidizing and Fe^{II}(Cp*)$_2$ reducing agents. The full description of the behaviors upon oxidation and reduction are done for the two representative complexes **4** and **7**.

Upon the addition of a $NOPF_6$ oxidizing agent for **4**, five new bands appear simultaneously with the disappearance of the HOMO → LUMO CT (DACT^1, 20750 cm^{-1}; Table 7 and Figure 11a). The lowest-energy bands were attributed to intramolecular CT (DACT^2, 11350 cm^{-1}; Table 7 and Figure 11c) but in the direction opposite to that of the neutral complex **4**. In analogy with previous work,[29] the main

dx.doi.org/10.1021/ic3010689 | Inorg. Chem. 2012, 51, 8488−8501

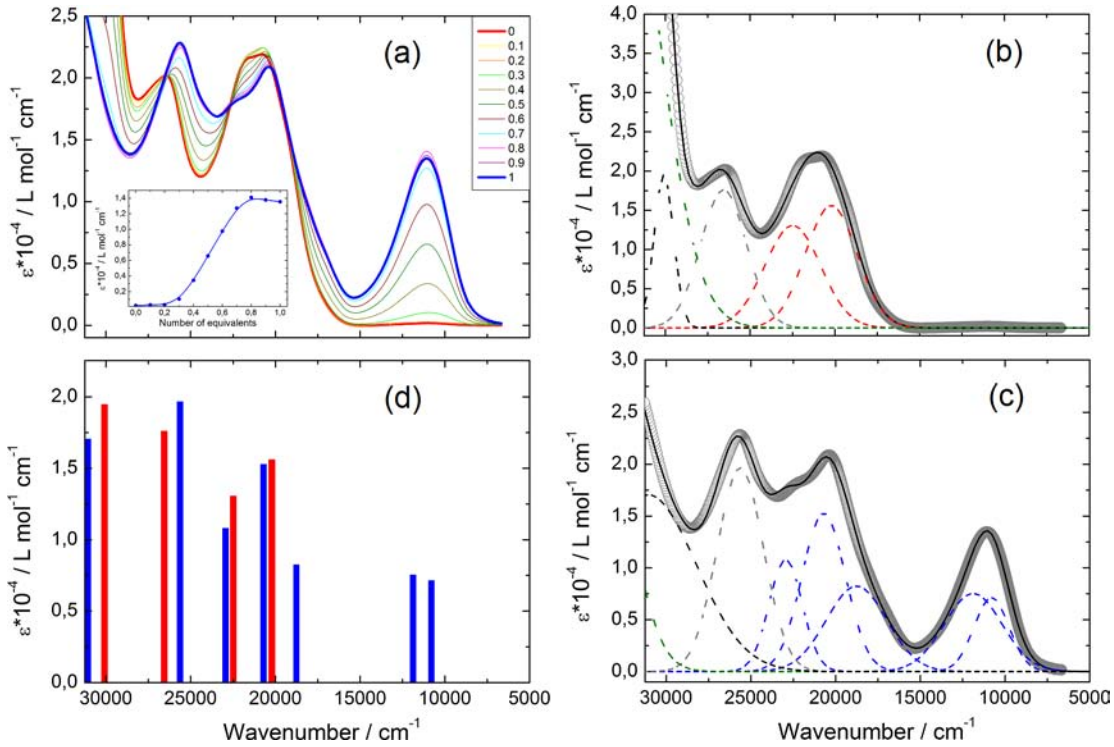

Figure 11. (a) Experimental dichloromethane solution (4×10^{-5} M) UV−visible absorption spectra upon the addition of a $NOPF_6$ oxidizing agent. Inset: intensity of the lowest-energy CT bands upon the addition of a $NOPF_6$ oxidizing agent and a number of added $NOPF_6$ equivalents. (b) Experimental dichloromethane solution (4×10^{-5} M) UV−visible absorption spectra of **4** (open gray circles), Gaussian deconvolutions (dashed lines), and best fit (full black line) (R = 0.9997). (c) Experimental dichloromethane solution (4×10^{-5} M) UV−visible absorption spectra of $\mathbf{4}^{\bullet+}$ (open gray circles), Gaussian deconvolutions (dashed lines), and best fit (full black line) (R = 0.9997). (d) Positions and intensities of the Gaussian deconvolutions for **4** (red sticks) and $\mathbf{4}^{\bullet+}$ (blue sticks).

contribution of DACT[2] is a monoelectronic SOMO−n → SOMO excitation from the salphen^{2-} moiety to the radical-cation TTF$^{\bullet+}$ core (where SOMO−n is a lower-energy orbital than SOMO). These CT excitations are allowed because of the strong decrease of the donating character of the radical-cation TTF$^{\bullet+}$ core compared to the neutral TTF core. In the same energy range of DACT[1] (red deconvolutions in the Figure 11b) appear three new absorption bands, which are attributed to a $\pi \rightarrow \pi^*$ intra-TTF$^{\bullet+}$ radical cation and to the SOMO → LUMO intramolecular CT. The SOMO and LUMO are respectively centered TTF$^{\bullet+}$ and salphen^{2-} orbitals (DACT[3], 20800 cm^{-1}; Table 7 and Figure 11c). The SOMO → LUMO CT of $\mathbf{4}^{\bullet+}$ is analogous to the HOMO → LUMO CT of **4**. The LMCT bands are red-shifted (1000 cm^{-1}) upon the addition of $NOPF_6$ (gray deconvolution; Table 7 and Figure 11a). This red shift can be attributed to energy destabilization of the bonding-centered ligand orbitals upon oxidation. The intrasalphen^{2-} excitation (IA, black deconvolution) remains almost at the same energy in **4** and $\mathbf{4}^{\bullet+}$ and attests that the phenol groups are not strongly affected by oxidation.

The average energy of the DACT[2] bands is almost the same for the free $\mathbf{L}^1$ (11300 cm^{-1}), the metallic precursor [($\mathbf{L}^1$)Ni] (11850 cm^{-1}), and **4** (11350 cm^{-1}). Consequently, it is not possible to conclude on the stability of the heterobimetallic complexes under oxidation, in particular whether the 4f ion remains coordinated or not. The presence of isosbestic points (Figure 11a) attests the equilibrium between only two species (**4** and $\mathbf{4}^{\bullet+}$) and may be a sign of the stability of the heterobimetallic complex under oxidation. The evolution of the intensity of DACT[3] upon the addition of $NOPF_6$ shows that oxidation is complete for 0.8−1 equiv of oxidizing agent, in agreement with the formula of **4** and the formation of $\mathbf{4}^{\bullet+}$. The reversibility of the oxidation was verified by the addition of the $Fe^{II}(Cp^*)_2$ reducing agent and the recovery of the neutral species **4**, in agreement with the electrochemical properties (Figure S4 in the Supporting Information).

The behaviors upon oxidation and reduction of the metallic precursors [($\mathbf{L}^1$)M] (Figures S10 and S11 in the Supporting Information) and the corresponding 3d4f heterobimetallic complexes (Figures 11 and S12 in the Supporting Information) are very similar. This is also the case for the dinuclear and tetranuclear complexes **4** and **7**.

For **7**, the reversible oxidation and reduction are complete after the addition of 2 equiv of $NOPF_6$ or $Fe^{II}(Cp^*)_2$ agents. Consequently, both $\mathbf{L}^2$ ligands are oxidized in the radical cation, and the oxidized species of **7** can be written as $\mathbf{7}^{2(\bullet+)}$ with simultaneous oxidation of both $\mathbf{L}^2$ ligands, in agreement with the electrochemical properties (Figure S4 in the Supporting Information).

Emission Properties. Upon excitation at 20850 cm^{-1} (480 nm) in the HOMO → LUMO CT transition, complex **4** exhibits a weak fluorescence band centered at 14450 cm^{-1} (692 nm) (Figure 10). The energy of the CT excited state can be estimated from the zero-phonon transition wavelength λ_{0-0} at 17850 cm^{-1} (560 nm) by averaging the energies of the lowest-energy absorption maximum and the highest-energy emission maximum. It is worth noting that CT excited states are known to present significant relaxation in their excited state, so the energy of the donating state is better described by the CT emission band taking into account its broadness.[30] In the

dx.doi.org/10.1021/ic3010689 | Inorg. Chem. 2012, 51, 8488−8501

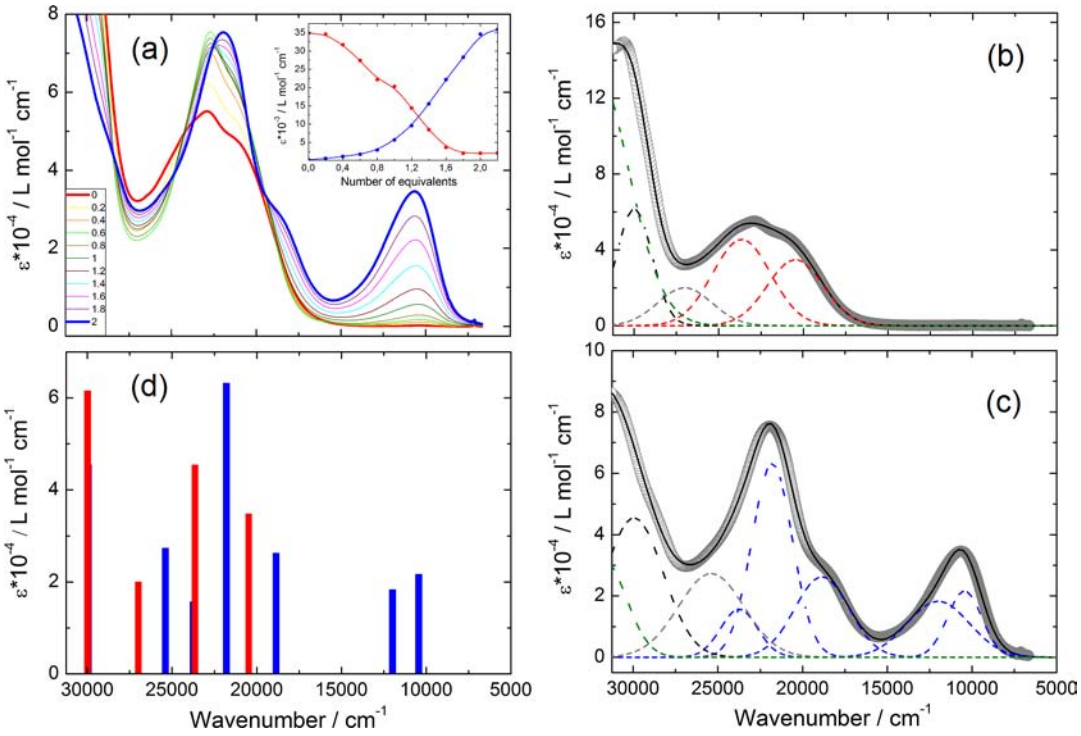

Figure 12. (a) Experimental dichloromethane solution (4×10^{-5} M) UV–visible absorption spectra upon the addition of a $NOPF_6$ oxidizing agent. Inset: intensity of the lowest-energy CT bands upon the addition of an oxidizing $NOPF_6$ (in blue) and a reducing $Fe^{II}(Cp^*)_2$ (in red) and number of added $NOPF_6$ equivalents. (b) Experimental dichloromethane solution (4×10^{-5} M) UV–visible absorption spectra of **7** (open gray circles), Gaussian deconvolutions (dashed lines), and best fit (full black line) (R = 0.9997). (c) Experimental dichloromethane solution (4×10^{-5} M) UV–visible absorption spectra of $7^{2(\bullet+)}$ (open gray circles), Gaussian deconvolutions (dashed lines), and best fit (full black line) (R = 0.9997). (d) Positions and intensities of the Gaussian deconvolutions for **7** (red sticks) and $7^{2(\bullet+)}$ (blue sticks).

Table 7. Experimental Absorption Data for L^1, $[Cu(L^1)]$, $[Ni(L^1)]$, and Selected Complexes[a]

	Neutral form (cm^{-1})			Oxidized form (cm^{-1})			
	DACT[1]	LMCT	IA	DACT[2]	ID + DACT[3]	LMCT	IA
L^1	25400	/	29900	11300	17300	/	30100
					24200		
$[Cu(L^1)]$	19900	26400	29900	10400	19000	26000	29900
	22800			12100	21600		
					23200		
$[Ni(L^1)]$	20300	26900	30000	10900	17800	25200	29700
	22600			12800	20600		
					22700		
(**3**)	19500	26900	30000	10400	18500	25600	30200
	22300			12300	21800		
					23800		
(**4**)	19500	26600	30100	10800	18800	25600	31100
	22000			11900	20700		
					22900		
(**7**)	20500	27000	30000	10400	18900	25400	29900
	23600			12000	21800		
					23700		

[a]LMCT = ligand-to-metal CTs, ID = intra-TTF donor excitations, IA = intra-salphen acceptor excitations, DACT[1] = TTF donor to $salphen^{2-}$ acceptor CTs, DACT[2] = $salphen^{2-}$ donor to $TTF^{\bullet+}$ acceptor CTs, and DACT[3] = $TTF^{\bullet+}$ donor to $salphen^{2-}$ acceptor CTs.

present case (Figure 10), the emission band starts with the zero-phonon transition (17850 cm^{-1}) and presents a maximum around 14450 cm^{-1}, and its red tail can be estimated at 9020 cm^{-1} using a rough deconvolution into the Gaussian function. The energy of the CT donation is in the 17850–9020 cm^{-1} range. Unfortunately, in solution and the solid state, at room temperature no luminescence centered on the 4f ions is observed in the case of **2**, **3**, **5**, and **6**.

CONCLUSIONS

Two easy synthetic procedures permitted access to two TTF-based ligands, L^1 and L^2. The former led to six heterobimetallic dinuclear complexes of the formula $[(L^1)MLn(hfac)_3]$ (where

dx.doi.org/10.1021/ic3010689 | Inorg. Chem. 2012, 51, 8488–8501

M = Cu^{II}, Ni^{II}; Ln = Y^{III}, Er^{III}, Yb^{III}), while the latter led to a heterobimetallic tetranuclear complex of the formula $[(\mathbf{L}^2)Cu(OH)Er(hfac)_3]_2$. A quantitative magnetic approach was performed using an homemade program considering a Hamiltonian including the crystal-field effects with the $\hat{O}_k^q$ operator equivalents, the Zeeman effect on the lanthanide, and spin-only magnetic moments that are coupled through *J*. Cu−Ln ferromagnetic interactions for Gd^{III} (1.29 cm^{-1}) and Tb^{III} (0.40 cm^{-1}) and antiferromagnetic interactions for Dy^{III} (−0.46 cm^{-1}) and Yb^{III} (−2.25 cm^{-1}) were determined, while in the case of Er^{III}, the magnetic interactions are negligible.

The UV−visible absorption properties for the neutral coordination complexes **1**−**7** were studied and rationalized by DFT and TD-DFT calculations for free $\mathbf{L}^1$, the metallic precursor $[(\mathbf{L}^1)Ni]$, and **4**. Thus, the lowest-energy absorption bands have been attributed to CTs from the TTF core to the salphen acceptor. Metalation by the Ni^{II} ion leads to stabilization of both HOMO (0.22 eV) and LUMO/LUMO +1 (0.66 eV) orbitals. Additional LMCTs and MLCTs involving the LUMO+2 ($d_{x^2-y^2}$) and HOMO−9 (d_{xz}) orbitals have appeared and have been identified. Finally, coordination of the $Y(hfac)_3$ moiety has provoked an additional red shift of the CT bands (HOMO → LUMO and HOMO → LUMO+1; 1850 cm^{-1}), demonstrating the good electronic communication along the whole ligand $\mathbf{L}^1$.

Upon the addition of $NOPF_6$, the TTF core of the ligand involved in $\mathbf{L}^1$, $[(\mathbf{L}^1)M]$, and complexes **3**, **4**, and **7** is oxidized in its radical-cation form. The $\mathbf{3}^{\bullet+}$, $\mathbf{4}^{\bullet+}$, and $\mathbf{7}^{2(\bullet+)}$ species show new intramolecular CT bands in the energy ranges of 11350 cm^{-1} (SOMO−*n* → SOMO DACT^2) and 20800 cm^{-1} (SOMO → LUMO DACT^3), while the HOMO → LUMO CT bands (DACT^1) of the respective neutral complexes disappear upon oxidation. The lowest-energy CTs are in the direction opposite to that of the neutral complexes, while the SOMO → LUMO CT of the oxidized complexes is analogous to the HOMO → LUMO CT of neutral ones. The reversibility of the oxidation was studied by cyclic voltammetry and UV−visible−NIR absorption properties upon the addition of a $[Fe^{II}(Cp^*)_2]$ reducing agent.

The irradiation of **4** at 20850 cm^{-1} induces the fluorescence of $\mathbf{L}^1$ at 14450 cm^{-1} with energy of the CT excited state of 17850 cm^{-1}.

Compound **7** is a promising system, and synthetic efforts to incorporate new 4f ions such as Tb^{III} and Dy^{III} are in progress in order to reach more interesting magnetic properties. The electrochemistry and absorption spectroscopy upon the addition of $NOPF_6$ support the possibility of obtaining single crystals of oxidized heterobimetallic coordination complexes to have electronic conductivity.

■ ASSOCIATED CONTENT

Supporting Information

Crystallographic information in CIF format, crystal packings for **3**, **4**, and **7** (Figures S1−S3), cyclic voltammetry for **2**, **5**, and **7** (Figure S4), $\chi_M(T)$ curve and best fit for **3** (Figure S5), energy level diagrams in the ground-state multiplet of Er^{III} for **2** and **5** (Figure S6), $\chi_M T$ vs *T* curves, best fits, and magnetic parameters for Tb^{III} and Dy^{III} analogues (Figures S7 and S8 and Table S1), $\chi_M T$ vs *T* and $M(H)$ curves for **7**, absorption spectra for $\mathbf{L}^1$, $[(\mathbf{L}^1)M]$ (M = Cu^{II}, Ni^{II}), and **3** (Figures S9−S12). This material is available free of charge via the Internet at http://pubs.acs.org.

■ AUTHOR INFORMATION

Corresponding Author

*E-mail: fabrice.pointillart@univ-rennes1.fr.

Notes

The authors declare no competing financial interest.

■ ACKNOWLEDGMENTS

This work was supported by the CNRS, Rennes Métropole, Université de Rennes 1, Région Bretagne, and FEDER. Dr. O. Maury is acknowledged for access to the fluorometer and his help with the measurements.

■ REFERENCES

(1) (a) Bryce, M. R. *Adv. Mater.* **1999**, *11*, 11. (b) Yamada, J.; Sugimoto, T. *TTF Chemistry: Fundamentals and applications of Tetrathiafulvalene*; Springer: Berlin, 2004. (c) Otsubo, T.; Takimiya, K. *Bull. Chem. Soc. Jpn.* **2004**, *77*, 43. (d) Kobayashi, A.; Fujiwara, E.; Kobayashi, H. *Chem. Rev.* **2004**, *104*, 5243. (e) Lorcy, D.; Bellec, N.; Fourmigué, M.; Avarvari, N. *Coord. Chem. Rev.* **2009**, *253*, 1398. (f) Shatruk, M.; Ray, L. *Dalton Trans.* **2010**, *39*, 11105. (g) Batail, P. *Chem. Rev.* **2004**, *104*, 4887.

(2) (a) Hansen, T. K.; Jørgensen, T.; Stein, P. C.; Becher, J. *J. Org. Chem.* **1992**, *57*, 6403. (b) Beer, P. D.; Gale, P. A.; Chen, G. Z. *J. Chem. Soc., Dalton Trans.* **1999**, 1897. (c) Bernhardt, P. V.; Moore, E. G. *Aust. J. Chem.* **2003**, *56*, 239. (d) Lu, H. Y.; Xu, W.; Zhang, D. Q.; Chen, C. F.; Zhu, D. B. *Org. Lett.* **2005**, *7*, 4629.

(3) (a) McCall, K. L.; Morandeira, A.; Durrant, J.; Yellowlees, L. J.; Robertson, N. *Dalton Trans.* **2010**, *39*, 4138. (b) Wenger, S.; Bouit, P.-A.; Chen, Q. L.; Teuscher, J.; Censo, D. D.; Humphry-Baker, R.; Moser, J.-E.; Delgado, J. L.; Martín, N.; Zakeeruddin, S. M.; Grätzel, M. *J. Am. Chem. Soc.* **2010**, *132*, 5164.

(4) (a) Spaldin, N. A.; Fiebig, M. *Science* **2005**, *309*, 391. (b) Eerenstein, W.; Mathur, N. D.; Scott, J. F. *Nature* **2006**, *442*, 759. (c) Train, C.; Gheorghe, R.; Krstic, V.; Chamoreau, L.-M.; Ovanesyan, N. S.; Rikken, G. L. J. A.; Gruselle, M.; Verdaguer, M. *Nat. Mater.* **2008**, *7*, 729. (d) Ouahab, L.; Enoki, T. *Eur. J. Inorg. Chem.* **2004**, 933.

(5) (a) Ojima, E.; Fujiwara, H.; Kato, K.; Kobayashi, H.; Tanaka, H.; Kobayashi, A.; Tokumoto, M.; Cassoux, P. *J. Am. Chem. Soc.* **1999**, *121*, 5581. (b) Fujiwara, H.; Ojima, E.; Nakazawa, Y.; Narymbetov, B.; Kato, K.; Kobayashi, H.; Kobayashi, A.; Tokumoto, M.; Cassoux, P. *J. Am. Chem. Soc.* **2001**, *123*, 306. (c) Kobayashi, H.; Sato, A.; Arai, E.; Akutsu, H.; Kobayashi, A.; Cassoux, P. *J. Am. Chem. Soc.* **1997**, *119*, 12392. (d) Tanaka, H.; Kobayashi, H.; Kobayashi, A.; Cassoux, P. *Adv. Mater.* **2000**, *12*, 1685. (e) Uji, S.; Shinagawa, H.; Terashima, T.; Terakura, C.; Yakabe, T.; Terai, Y.; Tokumoto, M.; Kobayashi, A.; Tanaka, H.; Kobayashi, H. *Nature* **2001**, *410*, 908. (f) Liu, S.-X.; Dolder, S.; Pilkington, M.; Decurtins, S. *J. Org. Chem.* **2002**, *67*, 3160. (g) Devic, T.; Avarvari, N.; Batail, P. *Chem.—Eur. J.* **2004**, *10*, 3697. (h) Liu, S.-X.; Dolder, S.; Franz, P.; Neels, A.; Stoeckli-Evans, H.; Decurtins, S. *Inorg. Chem.* **2003**, *42*, 4801. (i) Xue, H.; Tang, X.-J.; Wu, L.-Z.; Zhang, L.-P.; Tung, C.-H. *J. Org. Chem.* **2005**, *70*, 9727. (j) Massue, J.; Bellec, N.; Chopin, S.; Levillain, E.; Roisnel, T.; Clérac, R.; Lorcy, D. *Inorg. Chem.* **2005**, *44*, 8740. (k) Pellon, P.; Gachot, G.; Le Bris, J.; Marchin, S.; Carlier, R.; Lorcy, D. *Inorg. Chem.* **2003**, *42*, 2056. (l) Smucker, B. W.; Dunbar, K. R. J. *J. Chem. Soc., Dalton Trans.* **2000**, 1309. (m) Devic, T.; Batail, P.; Fourmigué, M.; Avarvari, N. *Inorg. Chem.* **2004**, *43*, 3136. (n) Avarvari, N.; Fourmigué, M. *Chem. Commun.* **2004**, 1300. (o) Iwahori, F.; Golhen, S.; Ouahab, L.; Carlier, R.; Sutter, J.-P. *Inorg. Chem.* **2001**, *40*, 6541. (p) Jia, C.; Liu, S.-X.; Ambrus, C.; Neels, A.; Labat, G.; Decurtins, S. *Inorg. Chem.* **2006**, *45*, 3152. (q) Ichikawa, S.; Kimura, S.; Mori, H.; Yoshida, G.; Tajima, H. *Inorg. Chem.* **2006**, *45*, 7575. (r) Wang, L.; Zhang, B.; Zhang, J. *Inorg. Chem.* **2006**, *45*, 6860. (s) Gavrilenko, K. S.; Le Gal, Y.; Cador, O.; Golhen, S.; Ouahab, L. *Chem. Commun.* **2007**, 280. (t) Cosquer, G.; Pointillart, F.; Le Gal, Y.; Golhen, S.; Cador, O.; Ouahab, L. *Dalton Trans.* **2009**, 3495. (u) Pointillart, F.; Le Gal, Y.; Golhen, S.; Cador,

O.; Ouahab, L. *Inorg. Chem.* **2008**, *47*, 9730. (v) Umezono, Y.; Fujita, W.; Awaga, K. *J. Am. Chem. Soc.* **2006**, *128*, 1084. (w) Setifi, F.; Ouahab, L.; Golhen, S.; Yoshida, Y.; Saito, G. *Inorg. Chem.* **2003**, *42*, 1791. (x) Pointillart, F.; Cauchy, T.; Le Gal, Y.; Golhen, S.; Cador, O.; Ouahab, L. *Inorg. Chem.* **2010**, *49*, 1947. (y) Kolotilov, S. V.; Cador, O.; Pointillart, F.; Golhen, S.; Le Gal, Y.; Gavrilenko, K. S.; Ouahab, L. *J. Mater. Chem.* **2010**, *20*, 9505.

(6) (a) Imakubo, T.; Sawa, H.; Tajima, H.; Kato, R. *Synth. Met.* **1997**, *86*, 2047. (b) Tamura, M.; Matsuzaki, F.; Nishio, Y.; Kajita, K.; Kitazawa, T.; Mori, H.; Tanaka, S. *Synth. Met.* **1999**, *102*, 1716. (c) Dyachenko, O. A.; Kazheva, O. N.; Gritsenko, V. V.; Kushch, N. D. *Synth. Met.* **2001**, *120*, 1017. (d) Otsuka, T.; Cui, H.; Kobayashi, A.; Misaki, Y.; Kobayashi, H. *J. Solid State Chem.* **2002**, *168*, 444. (e) Kushch, N. D.; Kazheva, O. N.; Gritsenko, V. V.; Buravov, L. I.; Van, K. V.; Dyachenko, O. A. *Synth. Met.* **2001**, *123*, 171. (f) Tamura, M.; Yamanaka, K.; Mori, K.; Nishio, Y.; Kajita, K.; Mori, H.; Tanaka, S.; Yamaura, J. I.; Imakubo, T.; Kato, R.; Misaki, Y.; Tanaka, K. *Synth. Met.* **2001**, *120*, 1041. (g) Pointillart, F.; Maury, O.; Le Gal, Y.; Golhen, S.; Cador, O.; Ouahab, L. *Inorg. Chem.* **2009**, *48*, 7421. (h) Pointillart, F.; Le Gal, Y.; Golhen, S.; Cador, O.; Ouahab, L. *Chem. Commun.* **2009**, 3777. (i) Faulkner, S.; Burton-Pye, B. P.; Khan, T.; Martin, L. R.; Wray, S. D.; Skabara, P. J. *Chem. Commun.* **2002**, *16*, 1668. (j) Pope, S. J. A.; Burton-Pye, B. P.; Berridge, R.; Khan, T.; Skabara, P.; Faulkner, S. *Dalton Trans.* **2006**, 2907. (k) Pointillart, F.; Le Gal, Y.; Golhen, S.; Cador, O.; Ouahab, L. *Inorg. Chem.* **2009**, *48*, 4631. (l) Pointillart, F.; Cauchy, T.; Maury, O.; Le Gal, Y.; Golhen, S.; Cador, O.; Ouahab, L. *Chem.—Eur. J.* **2010**, *16*, 11926. (m) Pointillart, F.; Le Gal, Y.; Golhen, S.; Cador, O.; Ouahab, L. *Chem.—Eur. J.* **2011**, *17*, 10397. (n) Pointillart, F.; Klementieva, S.; Kuropatov, V.; Le Gal, Y.; Golhen, S.; Cador, O.; Cherkasov, V.; Ouahab, L. *Chem. Commun.* **2012**, *48*, 714. (o) Pointillart, F.; Cauchy, T.; Maury, O.; Le Gal, Y.; Golhen, S.; Cador, O.; Ouahab, L. *Inorg. Chem.* **2012**, *51*, 978.

(7) Cosquer, G.; Pointillart, F.; Le Gal, Y.; Golhen, S.; Cador, O.; Ouahab, L. *Chem.—Eur. J.* **2011**, *17*, 12502.

(8) Carlin, R. L. *Magnetochemistry*; Springer: Berlin, 1986.

(9) For some recent reviews, see: (a) Winpenny, R. E. P. *Chem. Soc. Rev.* **1998**, *27*, 447. (b) Sakamoto, M.; Manseki, K.; Okawa, H. *Coord. Chem. Rev.* **2001**, *219*, 279. (c) Benelli., C.; Gatteschi, D. *Chem. Rev.* **2002**, *102*, 2369. (d) Sessoli, R.; Powell, A. K. *Coord. Chem. Rev.* **2009**, *253*, 2328. (e) Andruh, M.; Costes, J. P.; Diaz, C.; Gao, S. *Inorg. Chem.* **2009**, *48*, 3342 (Forum Article). (f) Andruh, M. *Chem. Commun.* **2011**, *47*, 3015. (g) Sorace, L.; Benelli, C.; Gatteschi, D. *Chem. Soc. Rev.* **2011**, *40*, 3092.

(10) Lempicki, A.; Samelson, H. *Phys. Lett.* **1963**, *4*, 133.

(11) (a) Bettencourt-Diaz, D. *Dalton Trans.* **2007**, 2229. (b) Kido, J.; Okamota, Y. *Chem. Rev.* **2002**, *102*, 2357.

(12) Burroughes, J. H.; Bradley, D. D. C.; Holmes, A. B. *Nature* **1990**, *347*, 539.

(13) Wu, J.-C.; Liu, S.-X.; Keene, T. D.; Neels, A.; Mereacre, V.; Powell, A. K.; Decurtins, S. *Inorg. Chem.* **2008**, *47*, 3452.

(14) Richardson, M. F.; Wagner, W. F.; Sands, D. E. *J. Inorg. Nucl. Chem.* **1968**, *30*, 1275.

(15) Sheldrick, G. M. *SHELX97—Programs for Crystal Structure Analysis*, release 97-2; Institüt für Anorganische Chemie der Universität: Göttingen, Germany, 1998. SIR97: Altomare, A.; Burla, M. C.; Camalli, M.; Cascarano, G. L.; Giacovazzo, C.; Guagliardi, A.; Moliterni, A. G. G.; Polidori, G.; Spagna, R. *J. Appl. Crystallogr.* **1999**, *32*, 115–119.

(16) Frisch, M. J.; Trucks, G. W.; Schlegel, H. B.; Scuseria, G. E.; Robb, M. A.; Cheeseman, J. R.; Scalmani, G.; Barone, V.; Mennucci, B.; Petersson, G. A.; Nakatsuji, H.; Caricato, M.; Li, X.; Hratchian, H. P.; Izmaylov, A. F.; Bloino, J.; Zheng, G.; Sonnenberg, J. L.; Hada, M.; Ehara, M.; Toyota, K.; Fukuda, R.; Hasegawa, J.; Ishida, M.; Nakajima, T.; Honda, Y.; Kitao, O.; Nakai, H.; Vreven, T.; Montgomery, J. A., Jr.; Peralta, J. E.; Ogliaro, F.; Bearpark, M.; Heyd, J. J.; Brothers, E.; Kudin, K. N.; Staroverov, V. N.; Kobayashi, R.; Normand, J.; Raghavachari, K.; Rendell, A.; Burant, J. C.; Iyengar, S. S.; Tomasi, J.; Cossi, M.; Rega, N.; Millam, J. M.; Klene, M.; Knox, J. E.; Cross, J. B.; Bakken, V.; Adamo, C.; Jaramillo, J.; Gomperts, R.; Stratmann, R. E.; Yazyev, O.; Austin, A. J.; Cammi, R.; Pomelli, C.; Ochterski, J. W.; Martin, R. L.; Morokuma, K.; Zakrzewski, V. G.; Voth, G. A.; Salvador, P.; Dannenberg, J. J.; Dapprich, S.; Daniels, A. D.; Farkas, O.; Foresman, J. B.; Ortiz, J. V.; Cioslowski, J.; Fox, D. J. *Gaussian 09*, revision A.02; Gaussian Inc.: Wallingford, CT, 2009.

(17) (a) Adamo, C.; Barone, V. *J. Chem. Phys.* **1999**, *110*, 6158–6170. (b) Ernzerhof, M.; Scuseria, G. E. *J. Chem. Phys.* **1999**, *110*, 5029.

(18) Dolg, M.; Stoll, H.; Preuss, H. *Theor. Chem. Acc.* **1993**, *85*, 441.

(19) Weigend, F.; Ahlrichs, R. *Phys. Chem. Chem. Phys.* **2005**, *7*, 3297.

(20) Tomasi, J.; Mennucci, B.; Cammi, R. *Chem. Rev.* **2005**, *105*, 2999.

(21) (a) Cossi, M.; Barone, V. *J. Chem. Phys.* **2001**, *115*, 4708. (b) Improta, R.; Barone, V.; Scalmani, G.; Frisch, M. J. *J. Chem. Phys.* **2006**, *125*, 054103.

(22) Allouche, A.-R. *J. Comput. Chem.* **2011**, *32*, 174.

(23) King, R. B. *J. Am. Chem. Soc.* **1969**, *91*, 7211.

(24) (a) Kahn, O. *Molecular Magnetism*; VCH: Weinheim, Germany, 1993. (b) Sutter, J.-P.; Kahn, M. L. *Magnetism: Molecules to materials V*; VCH: Weinheim, Germany, 2005.

(25) (a) Orbach, R. *Proc. Phys. Soc. A* **1961**, *264*, 458. (b) Rudowicz, C. *J. Phys. C: Solid State Phys.* **1985**, *18*, 1415.

(26) Gonçalves Silva, F. R.; Malta, O. L.; Reinhard, C.; Güdel, H. U.; Piguet, C.; Moser, J. E.; Bünzli, J.-C. G. *J. Phys. Chem. A* **2002**, *106*, 1670.

(27) (a) Costes, J.-P.; Dahan, F.; Wernsdorfer, W. *Inorg. Chem.* **2006**, *45*, 5. (b) Costes, J.-P.; Dahan, F.; Dupuis, A.; Laurent, J.-P. *Chem.—Eur. J.* **1998**, *4*, 1616. (c) Koner, R.; Lin, H.-H.; Wei, H.-H.; Mohanta, S. *Inorg. Chem.* **2005**, *44*, 3524.

(28) (a) Novitchi, G.; Wernsdorfer, W.; Chibotaru, L. F.; Costes, J.-P.; Anson, C. E.; Powell, A. K. *Angew. Chem., Int. Ed.* **2009**, *48*, 1614. (b) Benelli, C.; Caneschi, A.; Gatteschi, D.; Guillou, O.; Pardi, L. *Inorg. Chem.* **1990**, *29*, 1750. (c) Costes, J.-P.; Shova, S.; Wernsdorfer, W. *Dalton Trans.* **2008**, 1843.

(29) Jia, C.; Liu, S.-X.; Tanner, C.; Leiggener, C.; Neels, A.; Sanguinet, L.; Levillain, E.; Leutwyler, S.; Hauser, A.; Decurtins, S. *Chem.—Eur. J.* **2007**, *13*, 3804.

(30) D'Aleo, A.; Picot, P.; Beeby, A.; Williams, J. A. G.; Le Guennic, B.; Andraud, C.; Maury, O. *Inorg. Chem.* **2008**, *47*, 10258.